Article

Cell Reports

The branching code: A model of actin-driven dendrite arborization

Graphical abstract

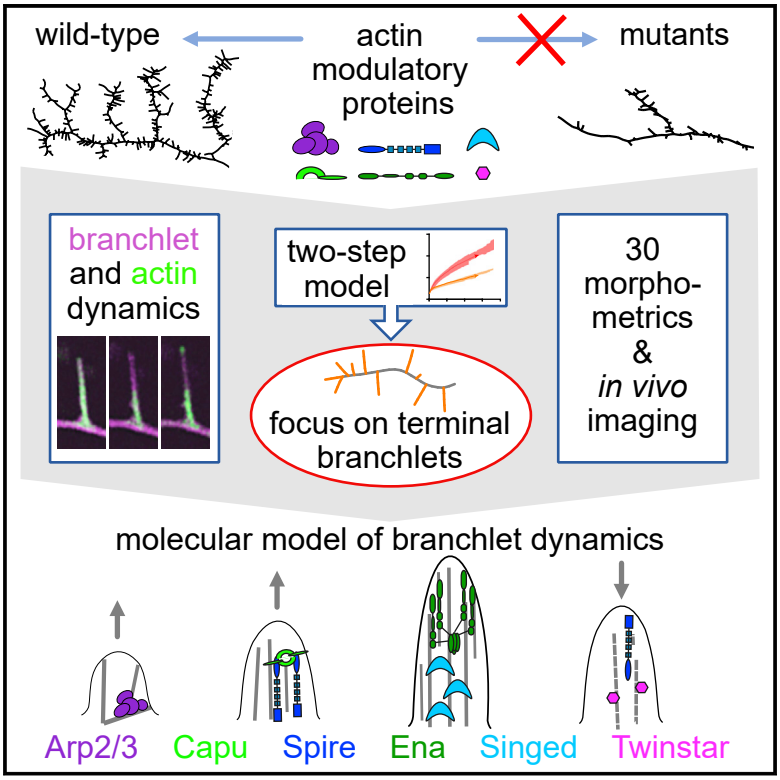

Highlights

- Oriented actin organization in short terminal branchlets of *Drosophila* c3da neurons
- AMPs individually control the characteristic morphology and dynamics of branchlets
- Quantitative tools for dendrite morphology and dynamics enable a comparative analysis
- c3da neurons utilize distinct growth models for different dendrite-branch types

Authors

Tomke Stürner, André Ferreira Castro, Maren Philipps, Hermann Cuntz, Gaia Tavosanis

Correspondence

cuntz@fias.uni-frankfurt.de (H.C.), gaia.tavosanis@dzne.de (G.T.)

In brief

Stürner et al. describe the involvement of 6 actin-modulatory proteins (AMPs) in different aspects of dendrite-branch morphology and dynamics in class III dendritic arborization neurons (c3da) of *Drosophila*. The comparative phenotypic analysis, integrating quantitative morphological features with computational modeling, provides a molecular model of dendritic-branch dynamics.

Stürner et al., 2022, Cell Reports *39*, 110746
April 26, 2022 © 2022
https://doi.org/10.1016/j.celrep.2022.110746

Cell Reports

CellPress
OPEN ACCESS

Article

The branching code: A model of actin-driven dendrite arborization

Tomke Stürner,[1,5] André Ferreira Castro,[1,2,3,6,7] Maren Philipps,[1] Hermann Cuntz,[2,3,8,*] and Gaia Tavosanis[1,4,8,9,*]
[1]German Center for Neurodegenerative Diseases (DZNE), 53127 Bonn, Germany
[2]Frankfurt Institute for Advanced Studies, 60438 Frankfurt am Main, Germany
[3]Ernst Strüngmann Institute (ESI) for Neuroscience in Cooperation with the Max Planck Society, 60528 Frankfurt am Main, Germany
[4]LIMES Institute, University of Bonn, 53115 Bonn, Germany
[5]Present address: Department of Zoology, University of Cambridge, Cambridge CB2 3EJ, UK
[6]Present address: Department of Physiology, Development and Neuroscience, University of Cambridge, Cambridge CB2 3DY, UK
[7]Present address: MRC Laboratory of Molecular Biology, Cambridge CB2 0QH, UK
[8]Senior author
[9]Lead contact
*Correspondence: cuntz@fias.uni-frankfurt.de (H.C.), gaia.tavosanis@dzne.de (G.T.)
https://doi.org/10.1016/j.celrep.2022.110746

SUMMARY

The cytoskeleton is crucial for defining neuronal-type-specific dendrite morphologies. To explore how the complex interplay of actin-modulatory proteins (AMPs) can define neuronal types *in vivo*, we focused on the class III dendritic arborization (c3da) neuron of *Drosophila* larvae. Using computational modeling, we reveal that the main branches (MBs) of c3da neurons follow general models based on optimal wiring principles, while the actin-enriched short terminal branches (STBs) require an additional growth program. To clarify the cellular mechanisms that define this second step, we thus concentrated on STBs for an in-depth quantitative description of dendrite morphology and dynamics. Applying these methods systematically to mutants of six known and novel AMPs, we revealed the complementary roles of these individual AMPs in defining STB properties. Our data suggest that diverse dendrite arbors result from a combination of optimal-wiring-related growth and individualized growth programs that are neuron-type specific.

INTRODUCTION

The morphology of dendrites is optimized to collect and process a neuron's input and is therefore exquisitely fitted to the specific needs of each neuron type (Jan and Jan, 2010; MacNeil and Masland, 1998). How the wide variety of neuron-type-specific dendrite morphologies is achieved is a key question in developmental neurobiology.

Morphological modeling can help dissect the growth principles shared among all dendrites from those that are more specific to individual neuron types (Cuntz, 2016; Poirazi and Papoutsi, 2020). In such an approach, synthetic morphologies are built from a set of assumptions made about branching statistics (Ascoli et al., 2001; Koene et al., 2009), wiring considerations (Budd et al., 2010; Cuntz et al., 2007, 2008, 2010), their underlying growth rules (Memelli et al., 2013; Palavalli et al., 2021; Sugimura et al., 2007; Torben-Nielsen and De Schutter, 2014), or even the computation that a given neuron is thought to implement (Ferreira Castro et al., 2020; Torben-Nielsen and De Schutter, 2014). In select cases, morphological modeling has elucidated the logic underlying structural plasticity of neuronal types during maturation (Beining et al., 2017) or after specific manipulations (Nanda et al., 2018a, 2018b, 2020; Sugimura et al., 2007; Yalgin et al., 2015).

Four morphologically and functionally distinct classes of dendritic arborization (da) neurons (c1da–c4da) extend their planar dendrites underneath the transparent cuticle of the *Drosophila* larva, facilitating *in vivo* imaging of their differentiation (Corty et al., 2009; Gao et al., 1999; Grueber et al., 2002, 2003; Tavosanis, 2021). Taking advantage of these properties, we recently designed a novel growth model fitted to the details of dendrite growth of c4da neurons during larval development and called it the space-filling growth tree (SFGT) model (Baltruschat et al., 2020). Based on well-established optimal-wiring-based models such as the minimal spanning tree (MST) model (Cuntz et al., 2007, 2008, 2010), SFGT replicates the time course of development while satisfying scaling relationships known in optimal-wiring models (Cuntz et al., 2012). The SFGT model accurately reproduces the branching behavior of c4da neurons and satisfies the mathematical aspects of dendrite morphological modeling derived from space-filling and optimal-wiring criteria. The SFGT model appears to generalize across different neuronal types, including dentate gyrus granule cells and cortical pyramidal neurons in various layers (Baltruschat et al., 2020). It also faithfully reproduces the initial phase of differentiation of c1da neurons in the fly larva (Ferreira Castro et al., 2020). Interestingly, however, a specialized, secondary growth program including a pruning phase was required to capture the mature morphology

of these c1da neurons and their development (Ferreira Castro et al., 2020; Palavalli et al., 2021). These findings prompted us to hypothesize that specialized dendrite morphologies could be achieved by a set of shared growth rules, reproduced in the optimal-wiring-related growth models MST and SFGT, complemented by specialized programs that are specific to individual neuronal types. Here, we tested this hypothesis by taking advantage of the well-characterized morphology of class III dendritic arborization (c3da) neurons of *Drosophila* larvae. c3da neurons, which respond to gentle touch and noxious cold (Tsubouchi et al., 2012; Turner et al., 2016; Yan et al., 2013), display long primary-dendrite branches (main branches [MBs]) decorated with characteristic short and dynamic terminal branchlets (STBs) that are required for gentle touch responses (Andersen, 2005; Grueber et al., 2002; Nagel et al., 2012; Tsubouchi et al., 2012; Yan et al., 2013). Interestingly, c3da STBs exhibit an unusual irregularity index, which characterizes the spatial distribution of dendritic branches, indicating that they may not match predictions derived from the SFGT model nor from the more broadly used MST algorithm (Anton-Sanchez et al., 2018). c3da neurons and their STBs appeared thus to represent an ideal system to interrogate the logic of neuron-type-specific dendrite morphology at the theoretical and molecular levels.

The structural and dynamic properties of cells are ultimately defined by the cytoskeleton (Coles and Bradke, 2015; Konietzny et al., 2017). The ensemble of numerous actin-modulatory proteins (AMPs), in particular, drives the dynamics that lead to dendritic-tree establishment (Lanoue and Cooper, 2019). Most key AMPs are highly conserved across species, and their biochemical properties have been carefully analyzed *in vitro* (Breitsprecher et al., 2008; Kovar et al., 2006; Mullins et al., 1998; Pruyne et al., 2002; Smith et al., 2013) and in cultured cells (Damiano-Guercio et al., 2020; Koestler et al., 2013; Suraneni et al., 2012; Wu et al., 2012). The collective activity of various AMPs produces different protrusion types (Schaks et al., 2019), and a recent study started addressing the coordination of multiple actin modulators in an *in vivo* system (Xie et al., 2021). However, how AMPs cooperate in space and time to form specialized dendritic morphologies during animal development *in vivo* is still highly speculative (Konietzny et al., 2017; Tavosanis, 2021).

Genetic studies have involved multiple cytoskeletal regulators in the establishment of da neuron dendrites *in vivo*. The actin-severing protein Twinstar/Cofilin regulates actin at dendrite-branching sites in c4da neurons, is localized at the base and along c3da STBs, and supports branch formation in all da classes (Nithianandam and Chien, 2018; Wolterhoff et al., 2020). The actin-nucleator complex Arp2/3 transiently localizes at branching sites, where it forms branched actin to initiate branchlet formation in all da neuron classes (Stürner et al., 2019). The actin barbed end-binding protein Ena/VASP promotes lateral branching of all da neuron classes (Dimitrova et al., 2008; Gao et al., 1999). While these AMPs seem to cover a general function in branch formation, the function of others is neuron-type specific. A striking example is afforded by the actin-bundling protein Singed/Fascin, which localizes exclusively within the highly actin-enriched STBs of c3da neurons and is required only in this distinctive type of branchlet (Grueber et al., 2002; Nagel et al., 2012). In addition, the actin-nucleation factor Spire is differentially regulated in c1da and c4da neurons (Ferreira et al., 2014). The latter studies indicate that individual subsets of branches, even within a neuron, contain specific AMPs defining their morphological and dynamic properties. Furthermore, they support, at the molecular level, our hypothesis of a core, general program supporting dendrite establishment, which is complemented by a neuron-type-specific secondary program to define the morphology of specific neuron types.

In this study, we investigated *in vivo* the complex molecular regulation of actin supporting the specific morphology and dynamics of c3da STBs. To achieve this, we performed an in-depth quantitative description of the morphological and dynamic phenotypes caused by the loss of function of key AMPs. Additionally, we revealed novel roles for two AMPs, Spire and Cappuccino (Capu). We further introduced a growth program model for STBs, which was required as a second step, following the optimal-wiring-based growth of MBs. Such a two-step growth model accurately replicates the characteristic wild-type c3da-neuron dendrite morphology, and we applied it to each of the mutants. We thus put forward a comprehensive model of actin-regulated control of c3da STB dynamics in the context of a two-step computational model of c3da-neuron morphology.

RESULTS

A two-step model is necessary to describe the c3da-neuron morphology

We used computational modeling as a first step toward understanding the characteristic morphology of c3da neurons and the growth rules that apply to their dendrite morphology. C3da neurons tile, covering 70% of the body wall, and scale during the larval growth phase, similar to c4da neurons (Grueber et al., 2002; Parrish et al., 2009). Therefore, we used the MST (Cuntz et al., 2007, 2010) and SFGT models (Baltruschat et al., 2020), which produce a space-filling coverage of the target area. MST-based modeling satisfies optimal-wiring constraints by balancing costs for total dendritic length and signal conduction times (Cuntz et al., 2007, 2010) (STAR Methods). The SFGT model shares the same optimal-wiring principles but with one simple parameter: the balancing factor (bf), representing the balance between total dendrite length and path length to the soma. In addition, in the SFGT model, a value for the stochasticity of innervation (k) accounts for irregular distributions of branches (Anton-Sanchez et al., 2018). On the basis of these two simple parameters, SFGT faithfully reproduces dendritic trees within any given planar or three-dimensional (3D) target spanning field (Baltruschat et al., 2020; Cuntz et al., 2008).

To model their morphology, we first imaged and traced control ldaB c3da neurons of early third-instar larvae (L3) *in vivo* (STAR Methods). We then let the SFGT model innervate the spanning field covered by the reconstructed c3da neurons, starting at the soma position (Figure 1A; STAR Methods). We first focused on the MBs of the c3da neuron by removing all STBs: first all terminal branches and then recursively all terminal branches shorter than 10 μm until none were left (Figure 1A, left). We found fitting parameters for the model with a bf of 0.1, a low k of 0.15, and a radius reach of 100 μm (STAR Methods). These parameters did not differ much from the model directly simulating

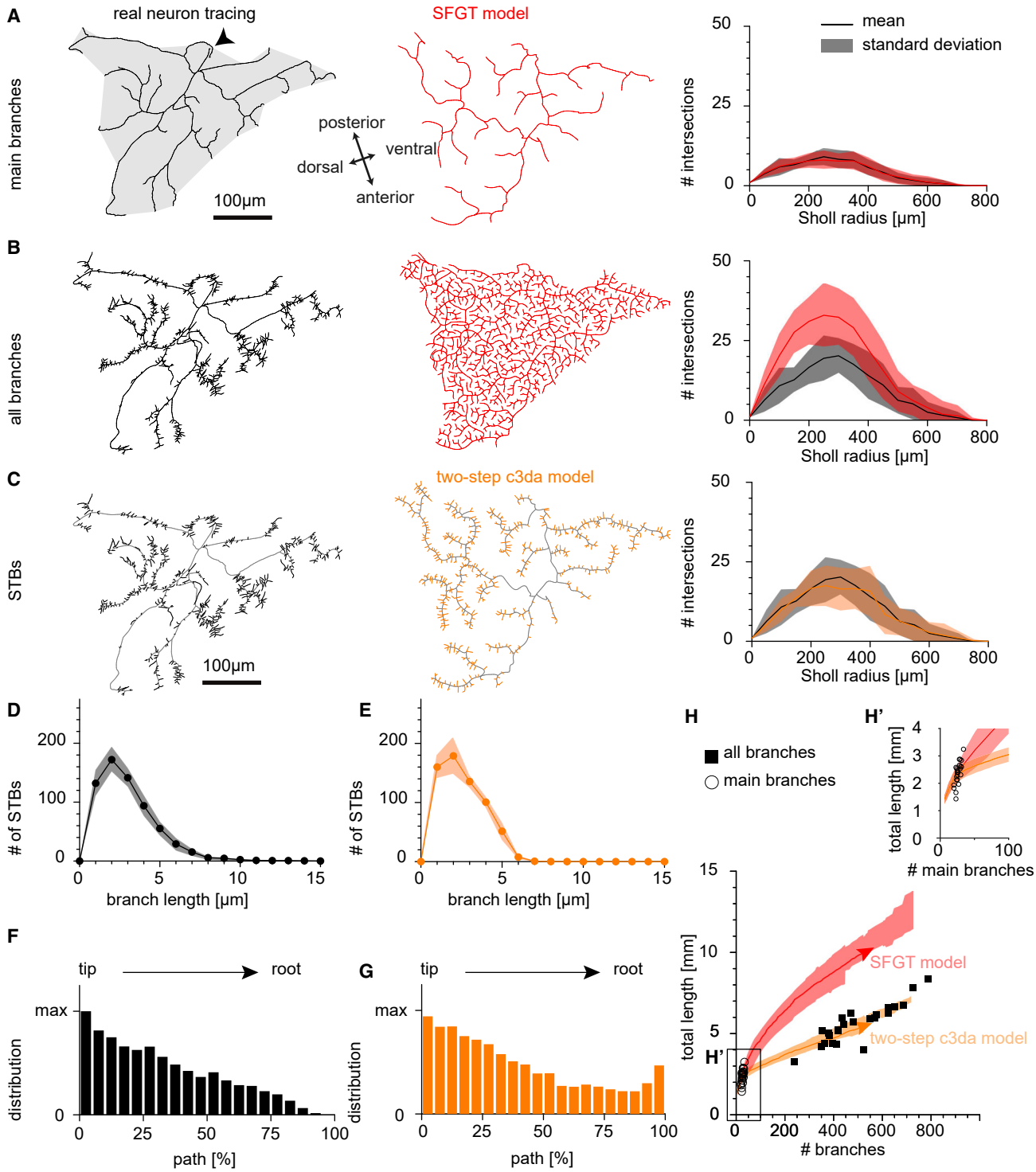

Figure 1. A two-step c3da model

(A–C) Tracings of a wild-type c3da neurons (black) with spanning field (shaded in gray) and synthetic dendritic trees (red or orange) focusing on the main branches (MBs; A), all branches (B), or the short terminal branches (STBs; C) (arrowhead in A points to the root). Right-hand Sholl-analysis panels: number of dendrite intersections with increasing Sholl radii distance from the soma (µm). Shaded area shows standard deviation, and solid lines show the mean. Scale bar: 100 µm.

(A and B) The red synthetic dendritic trees were generated with the SFGT model (Baltruschat et al., 2020), but the growth was interrupted when the number of MBs (A) or the total number of branches (B) was reached.

(C) The second modeling step allows STBs to grow with a defined total length and a given distribution along the MBs.

(legend continued on next page)

c4da-dendrite growth (Baltruschat et al., 2020). To obtain this, we stopped the simulated growth process when the number of branches reached the number of MBs in the corresponding real dendrite (Figure 1A, center). Total length and overall shape were then similar to the real counterparts (Figure 1A, right). However, when resuming growth in the model, the new branches filled the available space, failing to reproduce the characteristic STBs observed in c3da dendrites (Figure 1B). To confirm this finding, we utilized the same c3da-neuron traces to generate dendrites based on the MST model and the same fitting parameters as above (Figure S1; STAR Methods). Also, with the MST model, MB branching and distribution could be well reproduced (Figure S1A). The pattern of the branches subsequently added, though, did not resemble at all the characteristics of c3da STBs (Figure S1B).

Taken together, neither SFGT nor the classic MST model are sufficient to describe c3da neurons because of the number, shape, and distribution of their characteristic STBs. Modeling of these neurons thus seems to require a distinction between MBs and STBs. After preserving the MBs in accordance with the SFGT or the MST tree (Figures 1A, 1B, S1A, and S1B), we added STBs in a second growth phase. This second phase was intentionally kept as similar as possible to the SFGT or MST model to be able to identify the distinct differences between the STBs and MBs of c3da dendrites. It required different parameters bf = 0.625 and k = 0.5 and a much closer reach around the MBs that correlated with the distance to the root. Most importantly, STBs grew with a specific affinity toward the MBs rather than to the root of the entire dendrite, making this growth rule markedly distinct from other growth rules described previously (STAR Methods).

Informed only with the dendrite total length, the position of the soma, and the size and shape of the spanning field of the real dendrites (Figure 1A), this two-step model yielded dendrite trees that branched almost indistinguishably from the real counterparts, as demonstrated with Sholl-intersection diagrams (Figures 1C and S1C). The second step led to the replication of the characteristic branch-length distribution of STBs (Figures 1D and 1E) and to a similar distribution probability of the STBs along the MBs (Figures 1F, 1G, and S1D–S1H; STAR Methods). The c3da wild-type trees aligned with the growth trajectories obtained using this two-step c3da model with respect to the number of branches and the total length (Figures 1H and S1H), lying well off the trajectories predicted by the SFGT or MST model alone. Taken together, the two-step model captures the fundamental principles of c3da-neuron dendrite growth.

Actin organization in the STBs of c3da neurons

The model singled out the STBs as a second, neuron-type-specific level of dendrite elaboration of c3da neurons. STBs of c3da neurons are actin- and Singed/Fascin-enriched straight branchlets that dynamically extend and retract throughout larval stages (Nagel et al., 2012). To understand how precisely these branches are formed and how their dynamics are coordinated by AMPs, we first investigated the organization and dynamics of the actin cytoskeleton *in vivo*. To define the orientation of the actin filaments and their dynamic properties, we performed a fluorescence recovery after photobleaching (FRAP) analysis of green fluorescent protein (GFP)-labeled actin in the STBs of lateral c3da neurons (Figures 2A and 2B) (Röper et al., 2005; Verkhusha et al., 1999). Since *actin::GFP* is incorporated mainly at the fast-growing end of actin filaments, the site of GFP signal recovery provides an indication of the orientation of the filaments. For an internal reference, we also expressed a fluorescent, membrane-targeted chimeric protein highlighting the dendritic branchlet, enabling us to choose specifically extending STBs for FRAP analysis.

While the membrane-targeted chimera signal was almost unaffected, the *actin::GFP* signal dropped after photobleaching (Figures 2C and 2D; STAR Methods). We examined the recovery of the *actin::GFP* signal in the branchlet (Figures 2A–2C), after photobleaching the tips of elongating STBs (Figure 2B, white circle). Merely 30 s after photobleaching, the tip of the elongating dendritic branchlets displayed a sharp recovery of the *actin::GFP* signal at the distal end of the bleached area (Figure 2C, arrow). This indicated that the actin filaments in the c3da elongating STBs are mostly orientated with their fast-growing ends pointing distally.

We tracked the length and fluorescence intensity of the branchlet over time and measured the *actin::GFP* signal within the bleached area (*analysis_FRAP_macro.ijm*; Figures 2C–2E), revealing the velocity of actin turnover (half-time recovery $t^{1/2}$) and the speed of actin treadmilling (retrograde movement; Figure 2E) (Lai et al., 2008). The average half-time of recovery of *actin::GFP* in the bleached area was 2.5 min after photobleaching (Figure 2D; $t^{1/2}$) and full actin recovery in c3da STBs was around 5 min (Figure 2D). Thus, within the bleached area, the diffuse *actin::GFP* signal recovered slowly and evenly reported either on diffusion of G actin or on the fact that the actin bundle harbors actin filaments of different lengths (Figures 2C–2E). The retrograde treadmilling velocity of the bleached area measured in kymographs of *actin::GFP* fluorescence was r = 0.13 μm/min (Figure 2E). Taken together and given the enrichment of Singed/Fascin (Nagel et al., 2012), c3da STBs apparently contain mainly uniparallel actin bundles oriented with the majority of fast-growing ends pointing distally and displaying slow actin kinetics.

Analysis of six AMPs that regulate dendrite-branch number in c3da neurons

To ascertain the molecular regulation of actin in the c3da-neuron dendrites, we performed literature searches and a targeted screen of actin nucleators (Stürner et al., 2019), elongators, and bundling and depolymerization factors. We concentrated our analysis on mutants of six AMPs and imaged their c3da

(D and E) The number of STBs in the real neuron tracings (D) and the synthetic trees obtained with the two-step model (E) plotted against their length (μm).
(F and G) The number of STBs at positions along the MBs, from tip to root (percentile of MB path length).
(H) Number of branches versus total length for MBs (empty black dots, blown-up image in H′) and complete trees (black squares). Trajectories with standard deviation are shown for the SFGT (shaded red area) and two-step c3da (shaded orange area) models.
See Figure S1.

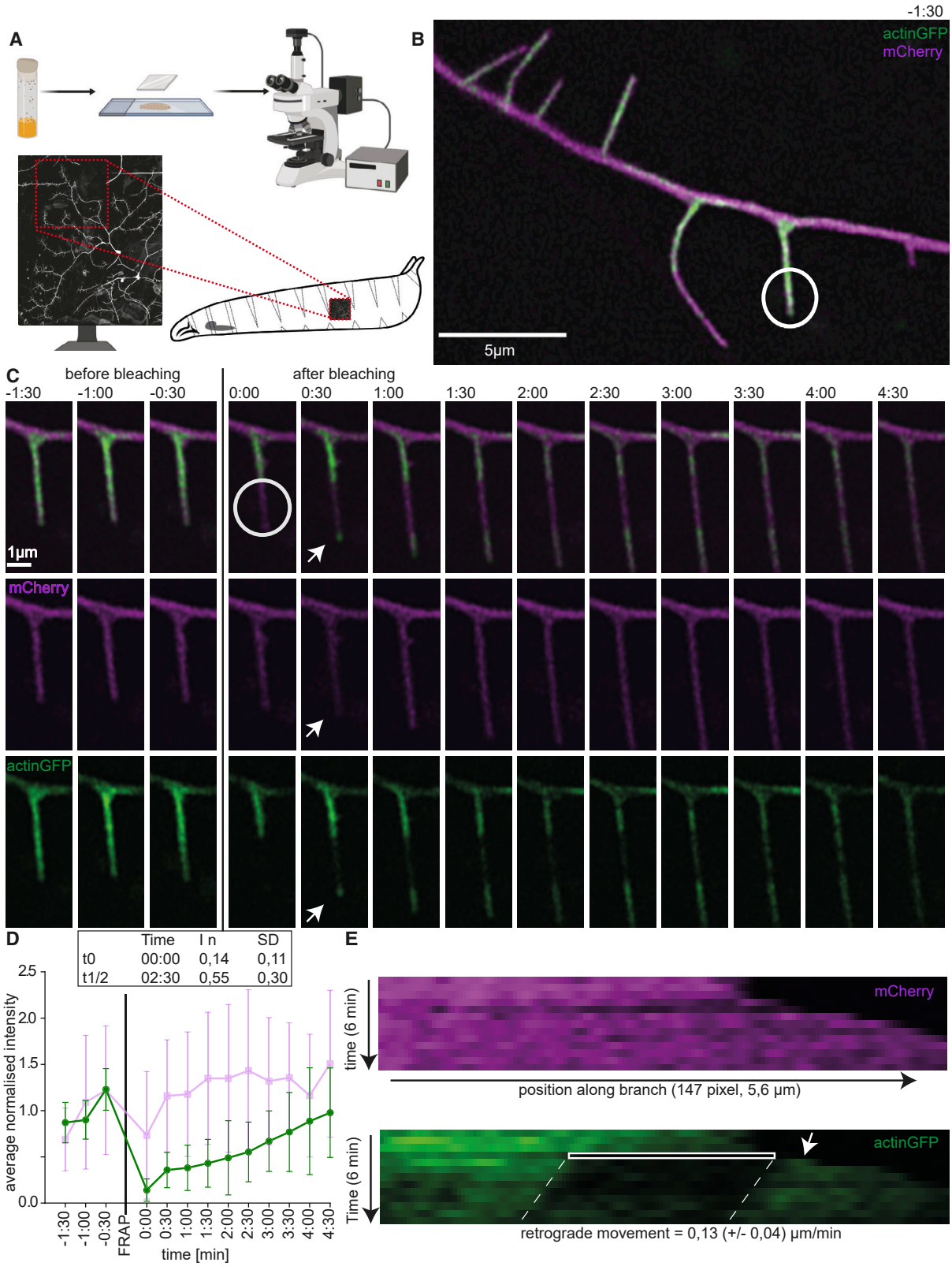

(legend on next page)

neurons *in vivo* at the early L3 stage (Figure 3A; STAR Methods). To extract a deep quantitative phenotypic description of their dendrite morphology, we traced and analyzed the c3da-neuron images in the TREES toolbox (Cuntz et al., 2010).

Single c3da clones (mosaic analysis with a repressible cell marker [MARCM]) (Lee and Luo, 1999) harboring a null mutation in a component of the essential actin nucleator Arp2/3 complex component *arpc1* (Figure 3B), a strong hypomorphic allele of the actin polymerase *ena* (Figure 3D), or a loss-of-function allele of the actin-severing factor *twinstar* (Figure 3D), as well as c3da neurons of larvae bearing a hypomorphic mutation for the actin-bundler *singed* (Figure 3F), all showed a reduced number of branches, as expected (Figures 3C, 3E, and 3G; Gao et al., 1999; Nagel et al., 2012; Nithianandam and Chien, 2018; Shimono et al., 2015; Stürner et al., 2019).

In addition, mutants of the actin nucleators *spire* or *capu* displayed total numbers of branches in c3da neurons that were reduced by roughly a third (Figures 3F, 3G, and S2). Thus, Spire and Capu represent novel regulators of c3da-neuron morphology (Figure S2). The cooperation of Spire and Capu is conserved across metazoa and extensively studied in *Drosophila* oocyte development (Dahlgaard et al., 2007). The trans-heterozygous combination of *spire* and *capu* mutants reduced the number of branches to a level comparable to that observed in the single homozygous mutants (Figure 3H), suggesting that Spire and Capu cooperate to define the number of c3da STBs.

Although each of these AMPs has a distinct biochemical function in actin organization, all mutants showed a reduced number of branches (Figure 3) in c3da neurons. To reveal potential distinctions that might allow for defining individual functions, we sought to define the morphology of wild-type c3da neurons and their STBs in greater detail.

Distinctive roles of six AMPs on c3da dendrites

As a second step toward a quantitative description of c3da-neuron dendrites and of the morphological effect of mutating individual AMPs, we identified a specific set of distinctive morphometric features for these neurons.

We collected 30 general dendritic-branching features (STAR Methods; Table 2; Ferreira Castro et al., 2020) and used them to quantitatively describe c3da dendrites (Table S1). We found that 13 of those features sufficed to accurately describe the differences between the AMP mutant c3da morphologies (Figures 4 and S3). The others were not significantly changed in any of the AMP mutant trees (5), were changed consistently in all AMP mutant trees (4), or were strongly correlated with already-chosen features (8) (Table S1).

In addition to the general reduction of STBs, *spire*, *capu*, and the transheterozygous *capu/spire* mutants showed a reduced number of MBs (Figures 4A and 4B). The mean length of MBs and STBs was unchanged, suggesting that *spire* and *capu* are important for the formation but not the elongation of these branches. Additionally, *capu*-mutant trees had a reduced mean Euclidean distance to the root and a reduced van Pelt asymmetry (illustration in Figure 4A), suggesting that Capu could also be involved in defining the position of new branches and their distance from the soma (Figure 4B).

The Arp2/3 complex is important for branch formation in all da-neuron classes (Stürner et al., 2019). *arpc1* mutant c3da neurons specifically lost STBs (Figure 3C), while the number of MBs did not change (Figure 4B). Moreover, the branches in *arpc1* mutants were more spread out, resulting in larger distances between neighboring terminal points and an increased surface area (Figure 4B). The STBs that were left had an increased tortuosity and were more evenly spread along the MBs (skewness of STBs along MBs). The lower van Pelt asymmetry value suggested that *arpc1* might be important for the general branching pattern in addition to contributing to the characteristic morphology of the STBs.

Ena encodes a substrate of the tyrosine kinase Abl, facilitating actin polymerization (Brühmann et al., 2017; Damiano-Guercio et al., 2020). c4da neurons display dendrite over-elongation and reduced branching in *ena* mutants (Dimitrova et al., 2008). Likewise, in *ena*-mutant c3da neurons, the loss of STBs was compensated in part by increasing the mean branch length of MBs and STBs to the point that the overall dendrite length was unchanged (Figure 4B), supporting the view that Ena might promote branching over elongation.

In hypomorphic mutants for the actin-bundling factor *singed*, the total length reduction of MBs and STBs in c3da dendrites was not compensated fully, to wild-type levels, by the increased mean length of STBs (Figure 4B), as is instead the case in null *singed* mutants (Nagel et al., 2012). The branches were more spread out, with increased distance between neighboring branches, but the total surface area was reduced (Figure 4B). The few branches that were left had an increased tortuosity, as shown previously (Nagel et al., 2012), and branched with larger branching angles (Figure 4B). Moreover, the van Pelt asymmetry and the skewness of STBs along MBs of the dendritic trees of the hypomorphic *singed* mutant were reduced (Figure 4B). These data are consistent with Singed/Fascin's role in defining the number and properties of the STBs (Nagel et al., 2012).

Figure 2. FRAP analysis of actin in c3da neuronal STBs

(A) Time-lapse imaging setup. ldaB STBs were chosen in a defined dendrite quadrant (red square) (BioRender.com).

(B) Representative overview image of a c3da dendritic branch 1 min before bleaching, membrane-mCherry (magenta), and actin::GFP (green). The white circle indicates the photobleached area at time point 0:00 of the time-lapse series. Scale bar: 5 μm.

(C) Time-lapse images of the same STB (B) every 30 s over a 6 min interval. Photobleached area at time point 0:00 (white circle). Bright GFP signal at the growing branchlet tip after photobleaching (white arrow). Scale bar: 1 μm.

(D) Average normalized actin::GFP (green) and membrane-mCherry (magenta) fluorescence intensity in the bleached area of 8 time series. Mean with standard deviation.

(E) Representative kymograph of the same dendritic branchlet over time and space. The bleached area (white rectangle) and retrograde movement (dashed white lines) of filamentous actin in this area. Actin::GFP recovery after photobleaching (white arrow). n = 8 neurons from individual larvae (STAR Methods; Table 1 for genotype).

See Video S1.

Table 1. Genotypes

Abbreviation	Genotype	Figure and pannel
	P{w[+mC] = UASp-GFP.Act5C}2-1/+; P{w[+mW.hs] = GawB}smid[C161], UAS−mCD8−Cherry/+	Figure 2, Video S1
control 40A	*P{w[+m*] = GAL4}5-40 P{w[+mC] = UAS-Venus.pm}1 P{w[+mC] = SOP-FLP}42; P{w[+mC] = tubP-GAL80}LL10 P{ry[+t7.2] = neoFRT}40A; P{w[+mC] = tubP-GAL80}LL10 P{ry[+t7.2] = neoFRT}40A/P{ry[+t7.2] = neoFRT}40A*	Figures 1A–1E, 1H, 3B, 3C, 4B, 5D,5E, 6D, S1A–S1C, S1F–S1H, S3D, S4A, S4B, and S4E
arpc1 q25sd (FBal0008422)	*P{w[+m*] = GAL4}5-40 P{w[+mC] = UAS-Venus.pm}1 P{w[+mC] = SOP-FLP}42; P{w[+mC] = tubP-GAL80}LL10 P{ry[+t7.2] = neoFRT}40A; P{w[+mC] = tubP-GAL80}LL10 P{ry[+t7.2] = neoFRT}40A/Arpc1[Q25sd] P{ry[+t7.2] = neoFRT}40A*	Figures 3B, 3C, 4B, 5D, 5E, 6D, S3D, S4A, S4B, and S4E
control G13	*P{w[+m*] = GAL4}5-40 P{w[+mC] = UAS-Venus.pm}1 P{w[+mC] = SOP-FLP}42; P{w[+mW.hs] = FRT(w[hs])}G13 P{w[+mC] = tubP-GAL80}LL2/P{w[+mW.hs] = FRT(w[hs])}G13*	Figures 1A–1E, 1H, 3D, 3E, 4B, 5B, 5C, 6E, 6G, S1A–S1C, S1F–S1H, S3E, S3G, S4A, S4B, and S4D
ena 210 (FBal0031206)	*P{w[+m*] = GAL4}5-40 P{w[+mC] = UAS-Venus.pm}1 P{w[+mC] = SOP-FLP}42; P{w[+mW.hs] = FRT(w[hs])}G13 P{w[+mC] = tubP-GAL80}LL2/P{w[+mW.hs] = FRT(w[hs])}G13 ena[210]*	Figures 3D, 3E, 4B, 5B, 5C, 6E, S3E, S4A, S4B, and S4D
twinstar N121 (FBal0177372)	*P{w[+m*] = GAL4}5-40 P{w[+mC] = UAS-Venus.pm}1 P{w[+mC] = SOP-FLP}42; P{w[+mW.hs] = FRT(w[hs])}G13 P{w[+mC] = tubP-GAL80}LL2/P{w[+mW.hs] = FRT(w[hs])}G13 tsr[N121]*	Figures 3D, 3E, 4B, 5B, 5C, 6G, S3G, S4A, S4B, and S4D
Control	*P{w[+mW.hs] = GawB}smid[C161],P{w[+mC] = UAS- mCD8::GFP.L}LL6/+*	Figures 1A–1E, 1H, 3A, 3F–3H, 4A, 4B, 5A, 5C, 6A–6C, 6F, S1A–S1C, S1F–S1H, S2A–S2D, S3A–S3C, S3F, S4A, S4B, and S4C
capu 1/EE (FBal0001537/ Fbal0045438)	*P{w[+mW.hs] = GawB}smid[C161],P{w[+mC] = UAS- mCD8::GFP.L}LL6/+; capu[EE] cn[1] bw[1]/capu[1] cn[1] bw[1]*	Figures 3F–3G, 4B, 5A–5C, 6B, S1C, S1D, S2C, S2D, S3A, S4A, S4B, and S4C
spire 1/2F (FBal0016011/ FBal0102386)	*P{w[+mW.hs] = GawB}smid[C161],P{w[+mC] = UAS- mCD8::GFP.L}LL6/+; spir[1] cn[1] bw[1]/b[1] pr[1] spir[2F] cn[1]*	Figures 3F–3G, 4B, 5A–5C, 6C, S1A, S1B, S2A, S2B, S3B, S4A, S4B, and S4C
capu 1/+	*P{w[+mW.hs] = GawB}smid[C161],P{w[+mC] = UAS- mCD8::GFP.L}LL6/+; capu[1] cn[1] bw[1]/+*	Figure 3H
spire 2F/+	*P{w[+mW.hs] = GawB}smid[C161],P{w[+mC] = UAS- mCD8::GFP.L}LL6/+; b[1] pr[1] spir[2F] cn[1]/+*	Figure 3H
capu 1/spire 2F	*P{w[+mW.hs] = GawB}smid[C161],P{w[+mC] = UAS- mCD8::GFP.L}LL6/+; capu[1] cn[1] bw[1]/b[1] pr[1] spir[2F] cn[1]*	Figures 3H and S3C
singed 3 (FBal0015773)	*sn[3]/sn[3]: P{w[+mW.hs] = GawB}smid[C161], P{w[+mC] = UAS- mCD8::GFP.L}LL6/+*	Figures 3F, 3G, 4B, 5A–5C, 6G, S3F, S4A, S4B, and S4C
UASspireHA	*P{w[+mW.hs] = GawB}smid[C161],P{w[+mC] = UAS- mCD8::GFP.L}LL6/M {UAS-spir.ORF.3xHA}ZH-86Fb; spir[1] cn[1] bw[1]/b[1] pr[1] spir[2F] cn[1]*	Figures S2A and S2B
UAScapu3MCherry	*P{w[+mW.hs] = GawB}smid[C161],P{w[+mC] = UAS- mCD8::GFP.L}LL6/P {pUAST-capu.3M.mCherry}; capu[EE] cn[1] bw[1]/capu[1] cn[1] bw[1]*	Figures S2C and S2D

The dendrites of the c3da neuron mutant for *twinstar* display the most severe reduction in STB and MB numbers (Figures 3D, 3E, and 4B) that were not compensated by the increased mean branch length of MBs and STBs yielding smaller trees, with decreased surface areas and smaller mean branching orders (Figure 4B). The branches left were more spread out, with increased distance between neighboring branches, increased branching angle, and decreased van Pelt asymmetry (Figure 4B). The few STBs left were more tortuous (Figure 4B). These data are consistent with a major role of Twinstar/Cofilin in branch formation, although some STBs were still present in these mutants, typically close to the cell body.

Taken together, a parallel evaluation of six AMP mutants pinpointed the 13 morphometric features of c3da neurons that best describe differences in dendrite morphology between these AMP mutants, suggesting that these might be important features of dendrite elaboration controlled by actin. Each of the AMPs affected the organization of the c3da neurons in characteristic ways, hinting at specific roles during dendrite elaboration.

The two-step c3da model can be applied to AMP mutant trees

Does the neuron grow with the same core rules established for wild-type c3da dendritic trees even in the AMP mutants,

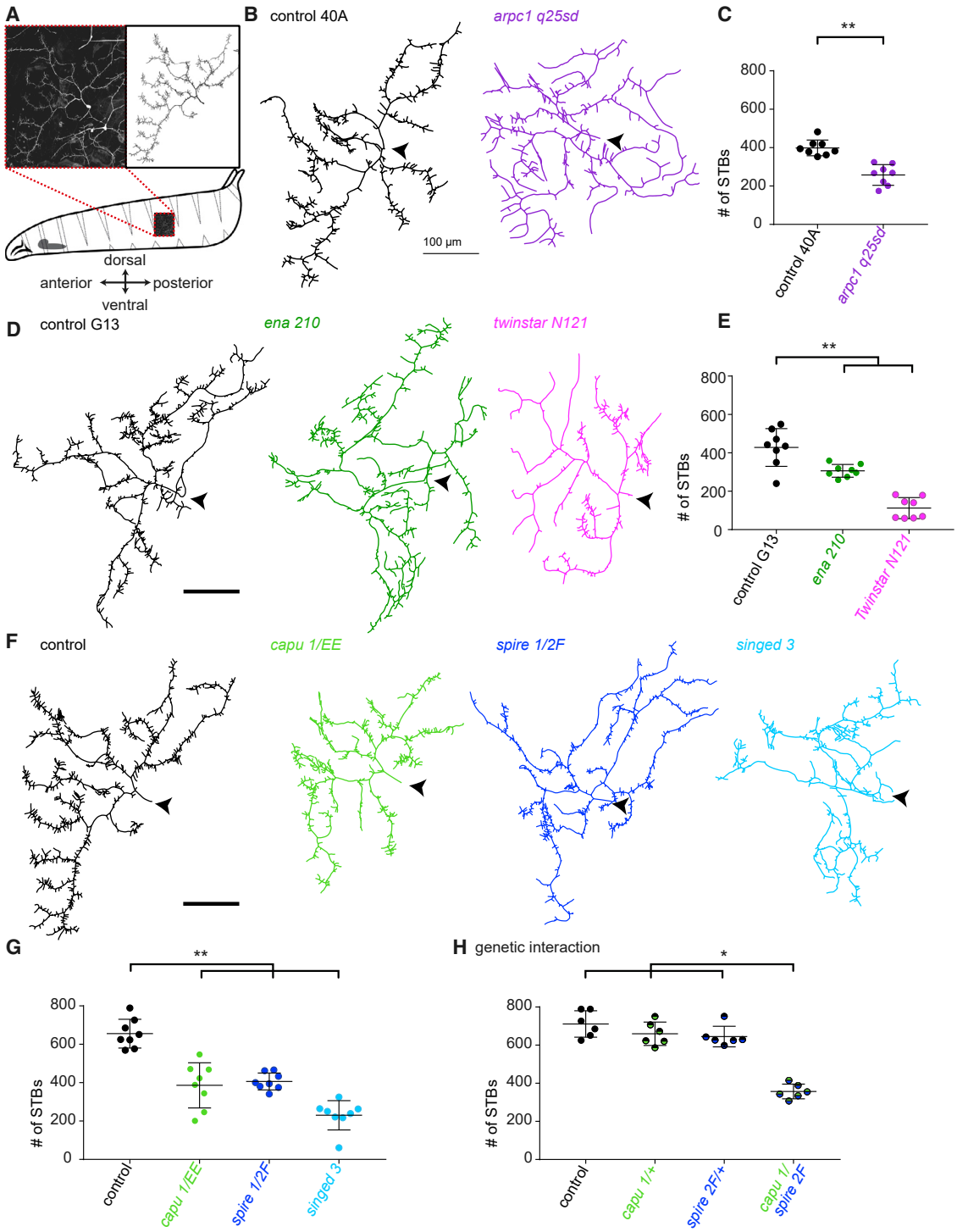

Figure 3. Actin-modulatory proteins involved in STB formation of c3da neurons

(A) Illustration of c3da-neuron imaging and tracing reconstructed in the TREES toolbox.

(B) Representative tracing of MARCM clones of control and arpc1^{q25sd} mutants.

(D) Representative tracing of MARCM clones of control, ena^{210}, or twinstar^{N121} mutants.

(F) Representative tracing of control, capu$^{1/EE}$, spire$^{1/2F}$, or singed^{3} mutants.

(legend continued on next page)

Table 2. 30 features with description

#	Name	Description
1	Number of STBs	Total number of terminal point indices in a tree. Equivalent to the total number of STBs.
2	Number of MBs	Total number of branches left after removing the STBs.
3	Total length of STBs	Sum of all length values of STB segments.
4	Total length of MBs	Sum of all length values of MB segments.
5	Mean length of STBs	Average of all length values of STB segments.
6	Mean length of MBs	Average of all length values of MB segments.
7	Mean branch order of STBs	Calculates the branch order of the tree and then takes the mean order for STBs.
8	Mean branch order of MBs	Calculates the branch order of the tree and then takes the mean order for MBs.
9	Mean tortuosity of STBs	Tortuosity is defined as ratio between Euclidean length and path length. Tortuosity of the STB segments of the tree.
10	Mean branching angle	Returns the mean of the angle at each branching point in degree.
11	Mean distance to nearest neighbor	Computes the distance of a branch or terminal point to the closest branch or terminal point.
12	Mean van Pelt asymmetry	Calculates the ratio of the sum of the daughter branches for each branching point and takes the mean.
13	Mean Euclidean distance to the root	Distance between all points of the tree and the root.
14	Surface	Calculates the area of the 2D spanning field.
15	Mean tortuosity of MBs	Tortuosity is defined as ratio between Euclidean length and path length. Tortuosity of the MB segments of the tree.
16	Number of branching points	Total number of branching point indices in a tree.
17	Maximal branch length of STBs	Computes all the STB lengths of the tree and takes the maximal length.
18	Fraction of lengths of STBs/total length	Density measure that takes the total length of STBs and divides it by the total length of the MBs.
19	Number of STBs/total length of MBs	Density measure that takes the total number of STBs and divides it by the total length of the MBs.
20	Minimal branch length of MBs	Computes all the MB lengths of the tree and takes the minimum length.
21	Maximal branch length of MBs	Computes all the MB lengths of the tree and takes the maximal length.
22	Maximal branch order of MBs	Calculates the branch orders of the tree and then takes the maximum order for the MBs.
23	Maximal branch order of STBs	Calculates the branch orders of the tree and then takes the maximum order for the STBs.
24	Maximal Euclidean distance to the root	The maximum distance of any terminal point on the tree and the root.
25	Mean Euclidean compactness	Euclidean distance to the root / (branch order +1).
26	Maximal path distance to the root	Calculates the total path to the root of each node of a tree and takes the maximum.
27	Mean path distance to the root	Calculates the total path to the root of each node of a tree and takes the mean.
28	Mean path compactness	Path distance to the root / (branch order +1).
29	Density	Total length divided by the surface area.
30	Skewness of STBs along MBs	Measures the asymmetry of the distribution of STB locations along the length of the MB from proximal to distal.

and, if so, can we predict the morphology of mutant dendritic trees? To resolve this question, we used the two-step model, with the bf, k, and outreach radius parameters defined for wild-type trees, to replicate the altered morphologies of the six AMP mutants.

We found that distributions of STB lengths in *singed*, *spire*, *capu*, *ena*, and *twinstar* mutants (Figures 5A–5C) were modeled adequately with the two-step c3da model, given their respective dendrite field areas and the total number of branches obtained from the real data of each individual mutant tree (Figure 3). The MBs, even in the highly reduced *twinstar* mutant (Figure S4A), were modeled adequately for the mutant neurons (Figure S4B). The distribution of STB lengths obtained from the model (orange dashed line) aligned with the distribution obtained from real dendritic trees (Figures 5A, 5B, S4C, and S4D). Moreover, the scaling relations in real dendritic trees of the different mutants corresponded well to the c3da model trajectories obtained in Figure 1 (Figure 5C and MBs in 5D). Thus, the two-step c3da model replicated branching statistics for these mutants

(C, E, and G) Quantification of total branch number.
(H) Total branch number in spire^{2F}/+, capu^{1}/+, or capu^{1}/spire^{2F} mutants. (*$p < 0.05$, **$p < 0.01$, and ***$p < 0.001$). Scale bar, 100 μm. n = 8 neurons from individual larvae per genotype (Table 1 for genotypes). Arrowheads point to the location of the soma.
See Figure S2 for rescue of the spire and capu-mutant phenotypes.

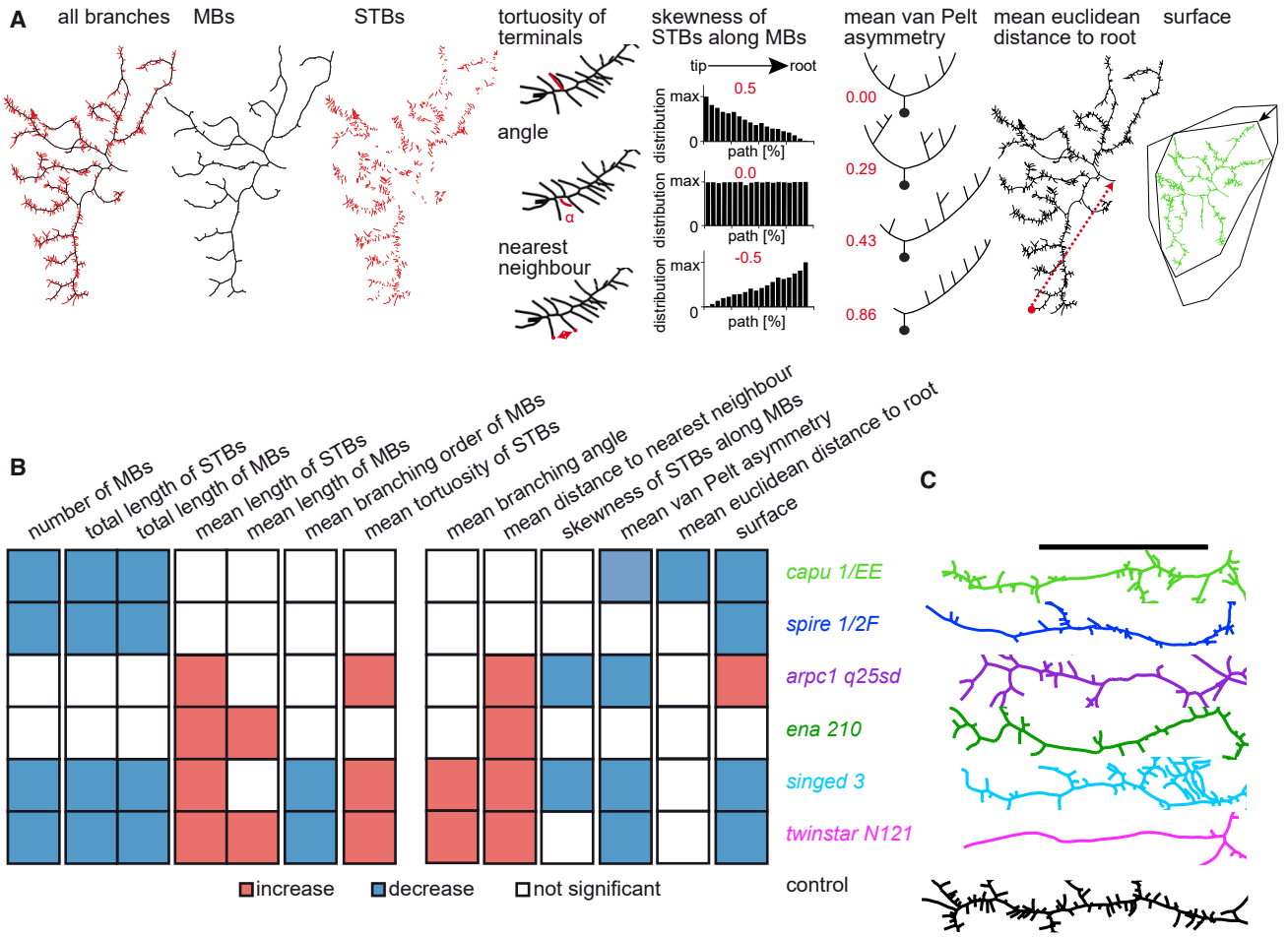

Figure 4. Features of dendritic-tree structure in c3da neurons

(A) Illustration of the 13 morphometric measures defining c3da neuronal morphologies. MBs (black) and STBs (red). Number of branches, total length, mean length, mean branching order, and mean tortuosity were calculated separately for MBs and STBs. The mean branching angle between branches, distance of terminal points to the nearest neighboring terminal point (μm), skewness of STBs along the MBs, mean van Pelt asymmetry, mean Euclidean distance to the root (to the soma), and surface area (area of a 2D spanning field) were measured for the entire dendritic tree.

(B) Analysis of the 13 morphological features for each mutant. Significant decrease (blue) and significant increase (red). n = 8 neurons from individual larvae per genotype.

(C) Images of one MB with STBs of the control and each mutant in corresponding colors (Table 1 for genotypes, and Table 2 for morphometric measures). Scale bar: 100 μm.

See Figure S3 for graphs and Table S1 for corrected p values.

without requiring any modifications of the parameters established for the wild type, i.e., none of the core growth rules used to build the two-step c3da growth model were altered in these mutants.

However, the *arpc1*-mutant dendritic trees could not be fully modeled with this two-step c3da model. While the spatial distribution of the MBs in the synthetic trees revealed by Sholl analysis resembled the wild type (Figures 5D and S4B), the distribution of the STB length in the model predicted shorter branches than observed in the real *arpc1*-mutant dendritic trees (Figures 5E and S4E). Thus, the two-step c3da model did not replicate the *arpc1*-mutant trees in their distribution of lengths of STBs nor in the correlation of total length to branch number (Figure 5F). The resulting scaling relationships as well as the longer STB lengths indicated that *arpc1*-mutant trees might lie somewhere between the c4da and the newly suggested c3da wild-type models (Figures 5E and 5F).

Taken together, the two-step c3da model was able to predict aspects of the dendritic-tree morphology of five out of six AMP mutants that we investigated. The c3da model does not include a detailed description of the morphological properties of STBs. Nonetheless, the wild-type c3da model directly predicted the length distributions of the STBs of five AMP mutants. This indicates that these five AMPs do not affect the core rules that define c3da dendrite distribution. In the case of the *arpc1*-mutant dendritic tree, however, the dendrite defect cannot be accurately modeled, suggesting that a core aspect of dendrite organization is altered in this mutant.

CellPress
OPEN ACCESS

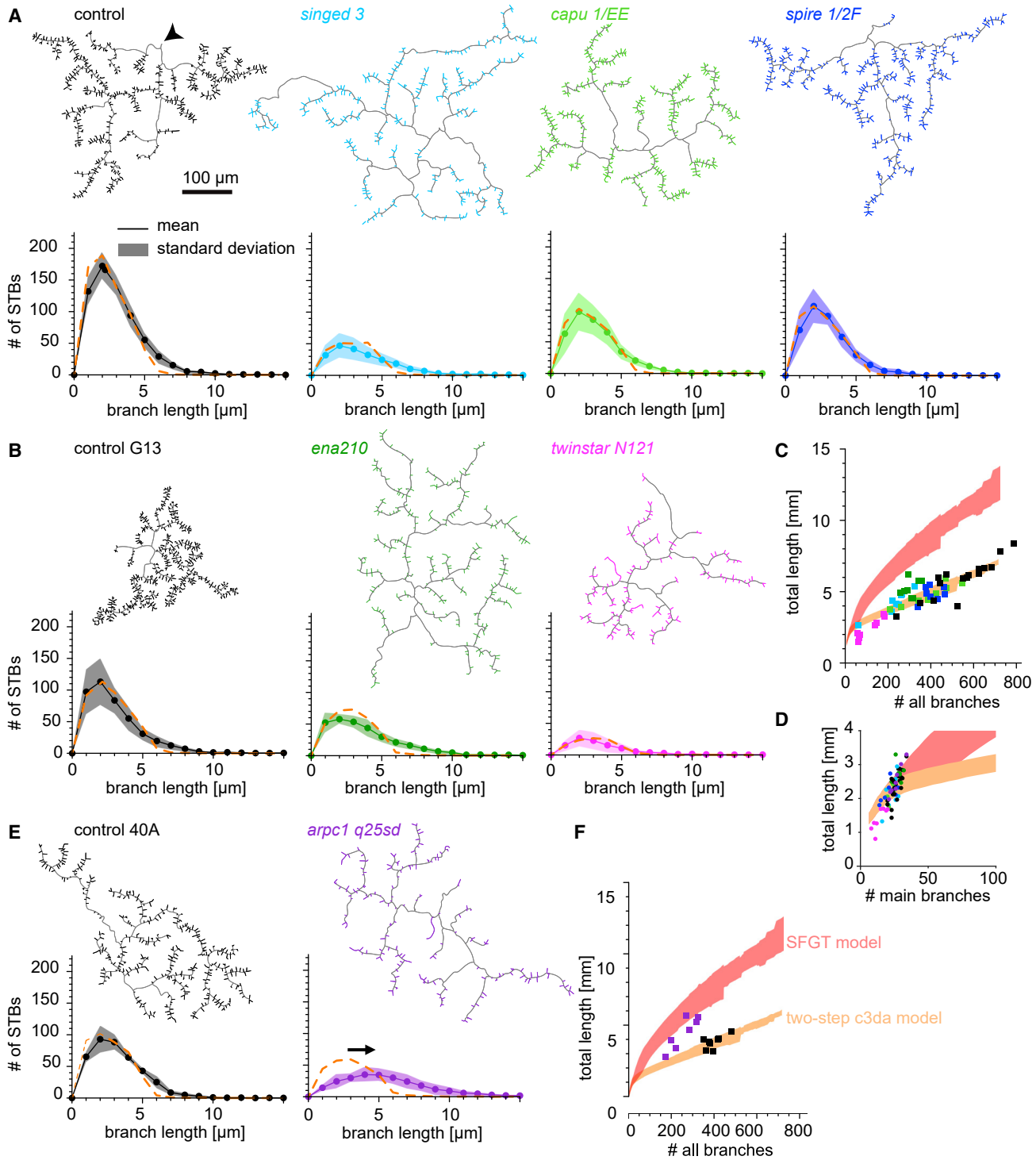

Figure 5. Modeling AMP mutant dendritic-tree morphology using the two-step model

(A, B, and E) The two-step c3da model applied to control and mutant dendritic trees; the STBs are represented in the color corresponding to the genotype. The distribution of branch lengths for all STBs is shown underneath each neuron tracing. Mean distributions from the model (orange dashed line) and real dendrites (color corresponding to the genotype) (Table 1 for genotypes). The arrow in (E) points to the shift observed in the *arpc1* mutant. Scale bar: 100 µm.

(C, D, and F) The real dendritic trees plotted with total length in mm to total number of branches. All branches (squares in C and F) or only MBs (colored dots in D). The trajectory for the c4da model is shaded red, and the trajectory for the c3da model is shaded in orange.

See Figure S4 for MST-based modeling version.

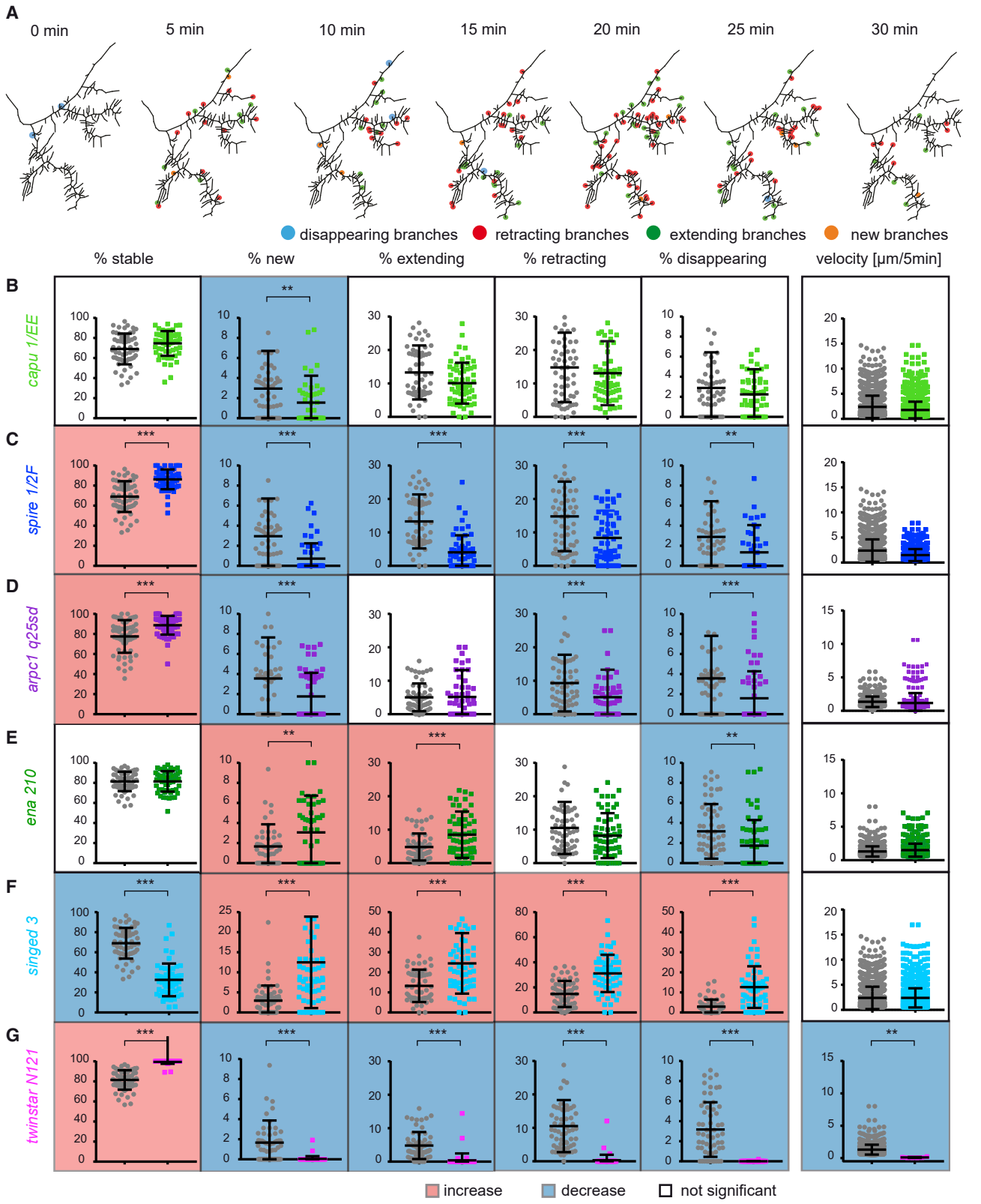

(legend on next page)

Contribution of individual AMPs to complex branchlet dynamics

There are different ways in which the reduction of dendritic branches and the specific alterations observed in the mutants could arise. For instance, the reduction of branches could be caused by defects in dendrite maintenance, by increased dendrite retraction, or by reduced branch formation. To gain a clearer understanding of the origin of morphological alterations observed in the different AMP mutants, we performed time-lapse analysis in live animals (STAR Methods). Immobilized late 2L were imaged every minute over 30 min. To simplify the analysis, we down-sampled to trace only every fifth minute and tracked the STBs over time using a dedicated user interface (Baltruschat et al., 2020) and *ad hoc* scripts (*ui_tlbp_tree*) in the TREES toolbox (www.treestoolbox.org), enabling us to compare the dynamics between animals and groups.

STBs were categorized into stable, new, extending, retracting, and disappearing branches, depending on the dynamics observed between one time point and the following, and were represented as the percentage of the total number of STBs (Figure 6A). We additionally tracked the terminal and branch points to measure the velocity of extension and retraction of branches (traveled distance of the branch tip in μm/5 min). Control STBs at this larval stage have a high proportion of stable branches (70%–80%, depending on the control). The remaining, dynamic branches extend and retract with an average velocity of 2–3 μm/5 min (Figures 6B–6G, gray). Interestingly, there are roughly the same percentage of STBs newly forming as disappearing within 30 min of imaging (2%–3%, between one time point and the next). The same is true for the percentage of STBs extending and retracting (5%–12%, between one time point and the next).

The loss of *capu*, *spire*, or *arpc1* led to a reduced number of newly forming branches (Figures 6B–6D), suggesting that these actin-nucleation factors are important for the very first step of branch formation, as previously demonstrated for *arpc1* (Stürner et al., 2019). In addition, mutants of *spire* showed an increase in stable branches that was linked to a decrease in the number of extending, retracting, and disappearing branches (Figure 6C). Thus, Spire displayed an additional role in branch dynamics, possibly linked to a function independent of Capu. The higher resolution of the time-lapse analysis in c3da neurons also suggested an additional, previously unrevealed, role for Arpc1 in promoting retraction and disappearance of branches, as both were decreased in the mutant conditions (Figure 6D; Stürner et al., 2019).

Time-lapse imaging of *ena* mutants at this larval stage revealed an increase in the percentage of STBs that were extending and newly forming as well as a reduction of disappearing branchlets in the absence of Ena (Figure 6E). While the high frequency of extending branches can explain the increase in mean length observed in the static images of *ena* mutants, the increase in newly forming and the decrease in disappearing STBs was unexpected and will need further investigation.

Singed/Fascin supports the formation of unipolar actin-filament bundles and is suggested to give filopodia the stiffness necessary for membrane protrusion (Vignjevic et al., 2006). Our improved time-lapse analysis revealed that this stiffness, although required for the characteristic straightness of the STBs, does not facilitate the dynamic movement of the branchlet (Figure 6F). A reduction in the amount of Singed/Fascin in the c3da neurons in fact led to an overall increase in dynamics, suggesting that the tight unipolar bundling of actin through Singed/Fascin might be restricting the dynamics of the branchlets (Figure 6F).

In partial agreement with recent data (Nithianandam and Chien, 2018) obtained by RNAi, the loss of *twinstar* showed almost no newly forming, extending, retracting, or disappearing branches in distal regions of the dendritic tree (Figure 6G). Thus, STB formation is very limited without actin remodeling through *twinstar*, and branch dynamics are strongly reduced.

Taken together, by examining the loss of individual AMPs in the same dendritic branchlet in a comparative way together with a detailed quantitative description of dynamics alterations in the AMP mutants, we could make a first attempt at understanding how, together, these AMPs define the specific dynamics of c3da STBs.

DISCUSSION

Neurons develop their dendrites in tight relation to their connection and computation requirements (Poirazi and Papoutsi, 2020). Thus, dendrite morphologies display sophisticated type-specific patterns. From the cell biological and developmental perspective, this raises the question of at which level different neuronal types might use shared mechanisms to assemble their dendrites. And, conversely, how are specialized structures achieved in different neuronal types? To start addressing these questions, we combined computational and comparative cell biological approaches. We found that two distinct growth programs are required to achieve models that faithfully reproduce the dendrite organization of c3da neurons. The models single out the STBs that are also molecularly identifiable as unique structures, displaying specific localization of actin and Singed. By combining time-lapse *in vivo* imaging and genetic analyses, we shed light on the machinery that controls the dynamic formation of those branchlets.

A molecular model of branchlet dynamics

The complex interplay of AMPs generates highly adaptive actin networks. In fact, in contrast to earlier unifying models, it is now clear that even the same cell can make more than one type of filopodium-like structure (Barzik et al., 2014; Bilancia

Figure 6. Time-lapse analysis of STBs of c3da neurons

(A) Representative example of a tracing of time-lapse images of a terminal region of a control c3da neuron over 30 min in 7 steps of 5 min. STBs that disappeared (blue), retracted (red), extended (green), or were newly formed (orange) from one time point to the next (dot in corresponding color).

(B–G) Percentage of STBs that were stable, new, extending, retracting, or disappearing between time points over 30 min for each mutant versus corresponding control (gray/black). Average velocity of an STB was quantified as the average change in length (extension + retraction) in μm/5 min (corrected p values: * $p < 0.05$, ** $p < 0.01$, and *** $p < 0.001$). Mean with standard deviation. Significant decrease (blue) and significant increase (red). n = 10 neurons from individual larva per genotype (see Table 1 for genotypes).

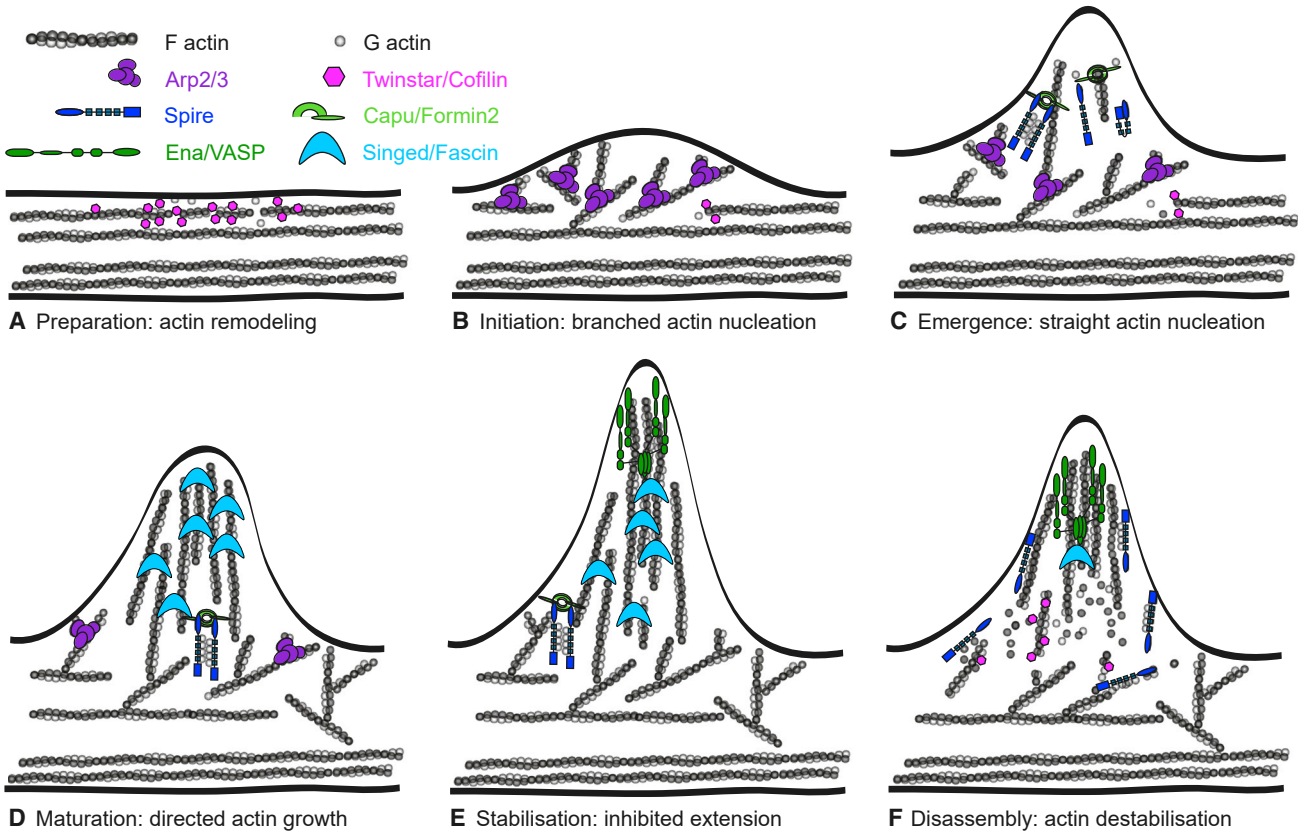

Figure 7. A theoretical model of dendritic branch dynamics

(A) Actin remodeling by Twinstar/Cofilin is a prerequisite for the formation of new filamentous-actin structures (F-actin).

(B) Membrane protrusion requires a branched actin network at the base, mediated by the actin-nucleation complex Arp2/3.

(C and D) Straight actin filaments, nucleated by Spire and Capu/Formin2 together, push out the membrane (C) before the actin filaments can be bundled by Singed/Fascin (D), restricting their dynamics and defining their characteristic angle and shape.

(E) Presence of Singed/Fascin facilitates the binding of Ena/VASP, which limits the STB from extending further.

(F) STBs regularly retract and can disappear completely, facilitated by Ena/VASP, Spire, and Twinstar/Cofilin.

et al., 2014). Here, we characterized the effect of the loss of six AMPs on the morphology and dynamics of one specific type of dendritic branchlet, the STB of c3da neurons. With this information, we delineate a molecular model for branchlet dynamics *in vivo* in the developing animal (Figure 7). Similar approaches to model the molecular regulation of actin in dendrite filopodia have been taken recently for cultured neurons (Marchenko et al., 2017). The advantage of the present approach is that it relies directly on the effect of the loss of individual AMPs *in vivo,* preserving the morphology, dynamics, and adhesive properties of the branchlets, and non-cell-autonomous signals remain present (Hogg et al., 2021; Tavosanis, 2021).

The combination of our FRAP experiments (Figure 2) and the localization of Singed/Fascin on the extending STBs (Nagel et al., 2012) indicated that actin is organized in a tight bundle of mostly uniparallel fibers in the STBs. This organization is thus very different from that of dendritic filopodia of hippocampal neurons in culture (Marchenko et al., 2017; Portera-Cailliau et al., 2003; Svitkina et al., 2010). The actin filaments in the bundle appear to be particularly stable in the c3da-neuron STBs, as the actin turnover that we revealed by FRAP analysis was 4 times slower than that reported in dendrite spines of hippocampal neurons *in vitro* (Star et al., 2002; Zito et al., 2004) and 20-fold slower than in a lamellipodium of melanoma cells *in vitro* (Lai et al., 2008). It is nonetheless in line with previous data on stable c3da-neuron STBs (Andersen, 2005) and with bundled actin filaments of stress fibers of human osteosarcoma cells (Hotulainen and Lappalainen, 2006). We observed treadmilling, similar to that of filopodia at the leading edge (Mallavarapu and Mitchison, 1999), with a retrograde flow rate 30 times slower than in filopodia of hippocampal cells (Chazeau et al., 2015) and comparable to rates observed for developing neurons in culture lacking the mammalian homologues of Twinstar and actin-depolymerization factor (ADF)/Cofilin (Flynn et al., 2012). Slower actin kinetics could be related to the fact that we are imaging neurons differentiating in the complex 3D context of a developing animal. Recent quantification of actin treadmilling in a growth cone of hippocampal neurons in 3D culture, however, did not produce differences with 2D-culture models (Santos et al., 2020).

The alterations of MB and STB morphology and dynamics caused by the loss of individual AMP functions reported here

can now be combined with preceding molecular knowledge about these conserved factors to produce a hypothetical model of the actin regulation underlying STB dynamics (Figure 7). Dendrite structure and time-lapse imaging point to an essential role of Twinstar/Cofilin for the initiation of a branchlet, in agreement with previous literature (Nithianandam and Chien, 2018) (Figure 7). *Drosophila* Twinstar/Cofilin is a member of the ADF/Cofilin protein family, with the capacity of severing actin filaments but with poor actin-filament-depolymerizing activity (Gunsalus et al., 1995; Shukla et al., 2018). We thus propose that Twinstar/Cofilin localized at the base of c3da STBs (Wolterhoff et al., 2020) can induce a local fragmentation of actin filaments that can then be used as substrate by the Arp2/3 complex. In fact, in c4da neurons, Arp2/3 localizes transiently at the site where the branchlets will be formed, and its presence strongly correlates with the initiation of branchlet formation (Stürner et al., 2019). Previous and present time-lapse data point to the role of Arp2/3 in the early phases of branchlet formation (Stürner et al., 2019) (Figure 6D). Thus, we suggest that localized activity of Arp2/3 generates a first localized membrane protrusion (Mogilner and Oster, 1996).

Given the transitory localization of Arp2/3 (Stürner et al., 2019), we have interrogated the role of additional actin nucleators in this context. From an RNAi-supported investigation, we identified Capu as potential modifier of c3da STBs (Stürner et al., 2019). Capu displays complex interactions with the actin-nucleator Spire during oogenesis, involving cooperative and independent functions of these two molecules (Dahlgaard et al., 2007). An increase in Spire levels correlates with a smaller dendritic tree and inappropriate, F-actin-rich, and shorter dendrites in c4da neurons (Ferreira et al., 2014). In our hands, though, the loss of Spire function did not yield a detectable phenotype in c4da neurons. In c3da neurons, we found that Capu and Spire support the formation of new branchlets and display a strong genetic interaction in the control of the number and length of MBs and STBs and surface area (Figures 4B and S3A–S3C). We thus suggest that they cooperatively take over the nucleation of linear actin filaments possibly producing the bundle of uniparallel actin filaments. Mutants for *capu* showed changes in the positioning of dendritic branches, not observed in *spire* mutants, which could mean that Capu localization defines the sites of Capu/Spire activity (Figure 4B). However, Spire seems to promote branch dynamics (Figure 6C), suggesting additional independent functions of Spire possibly not related to nucleation, given that Spire itself is a weak actin nucleator (Quinlan et al., 2007). While we do not have a clear indication *in vivo* for the molecular mechanisms supporting this function, an actin-severing activity of Spire was reported *in vitro* (Bosch et al., 2007). The role of Spire on STB dynamics appears to be consistent with favoring actin destabilization or actin dynamics (Figure 6C).

Singed/Fascin bundles actin filaments specifically in the c3da neuron STBs and gives these branches their straight conformation (Nagel et al., 2012). The localization of Singed/Fascin in the c3da STBs correlates with their elongation (Nagel et al., 2012). While the complete loss of *singed* function suppressed dynamics (Nagel et al., 2012), the mild reduction in protein levels analyzed here led to more frequent STB elongations and retractions. Further, the branchlets extended at the wrong angles and displayed a tortuous path (Figure 4B). Singed/Fascin controls the interaction of actin-filament bundles with Twinstar/Cofilin and can enhance Ena binding to barbed ends (Bachmann et al., 1999; Winkelman et al., 2014). Thus, in addition to generating mechanically rigid bundles (Mogilner and Rubinstein, 2005), it can modulate actin dynamics by regulating the interaction of multiple AMPs with actin. We speculate that the retraction and disappearance of the STB could be due to Singed/Fascin dissociating from the actin filaments, possibly in combination with Spire and Twinstar/Cofilin additionally severing actin filaments (Figure 7). In fact, the presence of detectable Twinstar/Cofilin along the c3da STBs was recently reported (Wolterhoff et al., 2020).

Ena is important for restricting STB length, and it inhibits the new formation and extension of STBs (Figures 4B and 6E). This appears to be a surprising function for Ena that is in contrast to its role in promoting actin-filament elongation (Barzik et al., 2005; Bear and Gertler, 2009; Breitsprecher et al., 2011; Hansen and Mullins, 2010; Krause et al., 2002; Pasic et al., 2008) or to its capacity of supporting the activation of the WAVE regulatory complex (Chen et al., 2014). Similar to what we previously reported for *ena*-mutant c4da neurons, we observe a balance between elongation and branching also in c3da neurons (Dimitrova et al., 2008). In *Drosophila* macrophages, Ena was shown to associate with Singed/Fascin within lamellipodia (Davidson et al., 2019). In line with these recent data, we suggest that Ena might closely cooperate with Singed to form tight actin bundles that slow down STB elongation.

Taken together, we put forward a comprehensive molecular model of dendrite-branch dynamics for the STBs of c3da neurons (Figure 7). In this analysis, we have excluded, for simplicity, the role of extracellular signals on the regulation of the dynamics of STBs. Nonetheless, such signals are likely to have a profound effect, particularly on the regulation of elongation and stabilization of STBs in relation to their target substrate. In addition, similar to what has been suggested for c1da neurons (Palavalli et al., 2021), the distribution of MBs in the target area might follow guidance cues that we have not included in the analysis, such as permissive signals that specifically guide c4da neurons to tile the body wall (Poe et al., 2017) or promote appropriate space filling (Hoyer et al., 2018).

Quantitative analysis of neuronal morphology

The investigation of morphological parameters in combination with genetic analysis has proven extremely powerful to reveal initial molecular mechanisms of dendrite differentiation (Gao and Bogert, 2003). Early studies, though, have been limited in the description power of their analysis concentrating on just one or two parameters (e.g., number of termini and total dendrite length). This limitation has been recognized and addressed in more recent studies (Das et al., 2017; Ferreira Castro et al., 2020; Kanaoka et al., 2019; Li et al., 2017; Nanda et al., 2018a; Palavalli et al., 2021; Sheng et al., 2018; Wang et al., 2019).

A major outcome of our present and previous work (Ferreira Castro et al., 2020) is the establishment of powerful tools for a thorough and comparative quantitative morphological analysis of different mutant groups. A detailed tracing of neuronal dendrites of the entire dendritic tree or a certain area of the tree in

a time series with a subsequent automatic analysis allows a precise description of mutant phenotypes. We additionally generated tools for extracting quantitative parameters of the dynamic behavior of dendrite branches from time-lapse movies based on a novel branch registration software (Baltruschat et al., 2020). This time-lapse tool operates similarly as in Sheng et al. (2018), was developed in parallel to Ferreira Castro et al. (2020), and yields an automated quantification after registration detecting branch types and their dynamics. Moreover, the tool operates in the same framework as the tracing and morphological analysis. We make these tools available within the TREES toolbox (www.treestoolbox.org) and encourage their use to support comparative analysis among datasets.

Specialized growth programs to refine individual-neuron-type dendrite morphology

What are the fundamental principles that define dendrite elaboration and which constraints need to be respected by neurons in establishing their complex arbors? Models based on local or global rules have been applied to reproduce the overall organization of dendritic trees, including da neurons (Baltruschat et al., 2020; Ferreira Castro et al., 2020; Nanda et al., 2018b; Palavalli et al., 2021). We based our c3da model on the fundamental organizing principle that dendrites are built through minimizing cable length and signal conduction times (Baltruschat et al., 2020; Cuntz et al., 2007, 2010; Wen and Chklovskii, 2008). This general rule for optimal wiring predicts tight scaling relationships between fundamental branching statistics, such as the number of branches, the total length, and the dendrite's spanning field (Cuntz et al., 2012).

Here, we found that c3da neurons respect the general developmental SFGT or MST models when stripped of all their STBs. However, the characteristic STBs of c3da dendrites did not follow this scaling behavior. Instead, a second growth program had to be applied to add the STBs to this basic structure, respecting their number, total length, and distribution. The two-step model developed in this work suggests that while main dendritic trees have common growth rules, the dendritic specializations of different neuronal cell types do not necessarily have the same constraints. This view is compatible with findings in a companion paper showing, in c1da neurons, a specialized branch-retraction step following an initial growth step (Ferreira Castro et al., 2020). In the two-step c3da dendrite model, the resulting synthetic morphologies resemble the real dendritic trees including those of five out of the six AMP mutant dendritic trees without any changes to the model parameters. The two-step model uses, for example, the reduced total length and reduced surface area of mutants for *singed* and *twinstar* and grows synthetic trees that have the same distribution of branch lengths and amounts as expected for those mutants. The synthetic trees corresponding to the *twinstar* mutant have less STBs than any other AMP mutant synthetic tree, consistent with the real mutant phenotypes.

Our work indicates that a combination of thorough statistical analysis (such as using the presented morphometrics) and models, like the one we developed here, can help capture the fundamental principles that govern dendrite differentiation (Hogg et al., 2021). Together with genetics analysis and systematic cell biology approaches, this type of study can deliver quantitative predictions for molecular models of dendrite elaboration.

In conclusion, we put forward the hypothesis that neuronal dendrites are built based on common, shared growth programs. An additional refinement step is then added to this scaffold, allowing each neuron type to specialize based on its distinctive needs in terms of number and distribution of inputs. In the exemplary case of c3da neurons, we investigated molecular properties of these more-specialized growth programs and propose a first comprehensive model of actin regulation that explains the morphology and dynamics of branchlets.

Limitations of the study

Most of the AMPs we study are essential, and all perform multiple functions during the course of development. Clearly, in our experiments, we have not isolated the acute function of each AMP in the process of STB formation and during STB dynamics. Rather, the progressive reduction of functional protein in MARCM clones or during the development of homozygous animals might represent a confounding factor (Copf, 2014; Lee and Luo, 1999; Long et al., 2009; Wang et al., 2020). In future studies, we will aim at using and developing tools for acute protein-function inactivation *in vivo* to add to our toolbox (Tavosanis, 2021).

STAR★METHODS

Detailed methods are provided in the online version of this paper and include the following:

- KEY RESOURCES TABLE
- RESOURCE AVAILABILITY
  - Lead contact
  - Materials availability
  - Data and code availability
- EXPERIMENTAL MODEL AND SUBJECT DETAILS
  - Fly strains
- METHOD DETAILS
  - Microscopy/live imaging
  - FRAP analysis
  - Dendritic arbor analysis
  - Time-lapse analysis
  - Computational modeling
- QUANTIFICATION AND STATISTICAL ANALYSIS

SUPPLEMENTAL INFORMATION

Supplemental information can be found online at https://doi.org/10.1016/j.celrep.2022.110746.

ACKNOWLEDGMENTS

We are grateful to Drs. F. Bradke, G. Marchetti, K. Rottner, P. Soba, B. Schaffran, and A. Ziegler for comments on the manuscript. This work was supported by a DFG grant (Teilprojekt, SPP 1464) to G.T. and a BMBF grant (no. 01GQ1406 — Bernstein Award 2013) and a DFG grant (CU217/2-1) to H.C. We thankfully acknowledge Dr. E. Kerkhoff and A. Samol-Wolf for the Capu construct and Dr. K. Rottner for discussion on the FRAP analysis. We thank R. Kerpen for great technical assistance.

AUTHOR CONTRIBUTIONS

T.S., A.F.C., M.P., H.C., and G.T. designed the study. T.S. performed the experiments. T.S. and A.F.C. designed and analyzed the time-lapse data. T.S. and M.P. made the graphical abstract. H.C. designed the growth models and performed the simulations. T.S., A.F.C., H.C., and G.T. wrote the paper.

DECLARATION OF INTERESTS

The authors declare no competing interests.

Received: June 24, 2021
Revised: December 24, 2021
Accepted: April 6, 2022
Published: May 3, 2022

REFERENCES

Andersen, R. (2005). Calcium/calmodulin-dependent protein kinase II alters structural plasticity and cytoskeletal dynamics in Drosophila. J. Neurosci. *25*, 8878–8888.

Anton-Sanchez, L., Effenberger, F., Bielza, C., Larrañaga, P., and Cuntz, H. (2018). A regularity index for dendrites - local statistics of a neuron's input space. PLoS Comput. Biol. *14*, e1006593.

Ascoli, G.A., Krichmar, J.L., Scorcioni, R., Nasuto, S.J., Senft, S.L., and Krichmar, G.L. (2001). Computer generation and quantitative morphometric analysis of virtual neurons. Anat. Embryol. (Berl.) *204*, 283–301.

Bachmann, C., Fischer, L., Walter, U., and Reinhard, M. (1999). The EVH2 domain of the vasodilator-stimulated phosphoprotein mediates tetramerization, F-actin binding, and actin bundle formation. J. Biol. Chem. *274*, 23549–23557.

Baltruschat, L., Tavosanis, G., and Cuntz, H. (2020). A developmental stretch-and-fill process that optimises dendritic wiring. Preprint at bioRxiv. https://doi.org/10.1101/2020.07.07.191064.

Barzik, M., Kotova, T.I., Higgs, H.N., Hazelwood, L., Hanein, D., Gertler, F.B., and Schafer, D.A. (2005). Ena/VASP proteins enhance actin polymerization in the presence of barbed end capping proteins. J. Biol. Chem. *280*, 28653–28662.

Barzik, M., McClain, L.M., Gupton, S.L., and Gertler, F.B. (2014). Ena/VASP regulates mDia2-initiated filopodial length, dynamics, and function. Mol. Biol. Cell *25*, 2604–2619.

Bear, J.E., and Gertler, F.B. (2009). Ena/VASP: towards resolving a pointed controversy at the barbed end. J. Cell Sci. *122*, 1947–1953.

Beining, M., Jungenitz, T., Radic, T., Deller, T., Cuntz, H., Jedlicka, P., and Schwarzacher, S.W. (2017). Adult-born dentate granule cells show a critical period of dendritic reorganization and are distinct from developmentally born cells. Brain Struct. Funct. *222*, 1427–1446.

Benjamini, Y., Krieger, A.M., and Yekutieli, D. (2006). Adaptive linear step-up procedures that control the false discovery rate. Biometrika *93*, 491–507.

Bilancia, C.G., Winkelman, J.D., Tsygankov, D., Nowotarski, S.H., Sees, J.A., Comber, K., Evans, I., Lakhani, V., Wood, W., Elston, T.C., et al. (2014). Enabled negatively regulates diaphanous-driven actin dynamics *in vitro and in vivo*. Dev. Cell *28*, 394–408.

Bosch, M., Le, K.H.D., Bugyi, B., Correia, J.J., Renault, L., and Carlier, M.-F. (2007). Analysis of the function of spire in actin assembly and its synergy with formin and profilin. Mol. Cell *28*, 555–568.

Brand, A.H., and Perrimon, N. (1993). Targeted gene expression as a means of altering cell fates and generating dominant phenotypes. Dev. Camb. Engl. *118*, 401–415.

Breitsprecher, D., Kiesewetter, A.K., Linkner, J., Urbanke, C., Resch, G.P., Small, J.V., and Faix, J. (2008). Clustering of VASP actively drives processive, WH2 domain-mediated actin filament elongation. EMBO J. *27*, 2943–2954.

Breitsprecher, D., Kiesewetter, A.K., Linkner, J., Vinzenz, M., Stradal, T.E.B., Small, J.V., Curth, U., Dickinson, R.B., and Faix, J. (2011). Molecular mechanism of Ena/VASP-mediated actin-filament elongation: actin-filament elongation by Ena/VASP. EMBO J. *30*, 456–467.

Brühmann, S., Ushakov, D.S., Winterhoff, M., Dickinson, R.B., Curth, U., and Faix, J. (2017). Distinct VASP tetramers synergize in the processive elongation of individual actin filaments from clustered arrays. Proc. Natl. Acad. Sci. *114*, E5815–E5824.

Budd, J.M.L., Kovács, K., Ferecskó, A.S., Buzás, P., Eysel, U.T., and Kisvárday, Z.F. (2010). Neocortical axon arbors trade-off material and conduction delay conservation. PLoS Comput. Biol. *6*, e1000711.

Chazeau, A., Garcia, M., Czöndör, K., Perrais, D., Tessier, B., Giannone, G., and Thoumine, O. (2015). Mechanical coupling between transsynaptic N-cadherin adhesions and actin flow stabilizes dendritic spines. Mol. Biol. Cell *26*, 859–873.

Chen, X.J., Squarr, A.J., Stephan, R., Chen, B., Higgins, T.E., Barry, D.J., Martin, M.C., Rosen, M.K., Bogdan, S., and Way, M. (2014). Ena/VASP proteins cooperate with the WAVE complex to regulate the actin cytoskeleton. Dev. Cell *30*, 569–584.

Coles, C.H., and Bradke, F. (2015). Coordinating neuronal actin–microtubule dynamics. Curr. Biol. *25*, R677–R691.

Copf, T. (2014). Developmental shaping of dendritic arbors in Drosophila relies on tightly regulated intra-neuronal activity of protein kinase A (PKA). Dev. Biol. *393*, 282–297.

Corty, M.M., Matthews, B.J., and Grueber, W.B. (2009). Molecules and mechanisms of dendrite development in *Drosophila*. Development *136*, 1049–1061.

Cuntz, H. (2016). Modeling Dendrite Shape. In Dendrites, G. Stuart, N. Spruston, and M. Häusser, eds. (Oxford University Press), pp. 487–504.

Cuntz, H., Borst, A., and Segev, I. (2007). Optimization principles of dendritic structure. Theor. Biol. Med. Model. *4*, 21.

Cuntz, H., Forstner, F., Haag, J., and Borst, A. (2008). The morphological identity of insect dendrites. PLoS Comput. Biol. *4*, e1000251.

Cuntz, H., Forstner, F., Borst, A., and Häusser, M. (2010). One rule to grow them all: a general theory of neuronal branching and its practical application. PLoS Comput. Biol. *6*, e1000877.

Cuntz, H., Mathy, A., and Hausser, M. (2012). A scaling law derived from optimal dendritic wiring. Proc. Natl. Acad. Sci. *109*, 11014–11018.

Dahlgaard, K., Raposo, A.A.S.F., Niccoli, T., and St Johnston, D. (2007). Capu and spire assemble a cytoplasmic actin mesh that maintains microtubule organization in the Drosophila oocyte. Dev. Cell *13*, 539–553.

Damiano-Guercio, J., Kurzawa, L., Mueller, J., Dimchev, G., Schaks, M., Nemethova, M., Pokrant, T., Brühmann, S., Linkner, J., Blanchoin, L., et al. (2020). Loss of Ena/VASP interferes with lamellipodium architecture, motility and integrin-dependent adhesion. Elife *9*, e55351.

Das, R., Bhattacharjee, S., Patel, A.A., Harris, J.M., Bhattacharya, S., Letcher, J.M., Clark, S.G., Nanda, S., Iyer, E.P.R., Ascoli, G.A., et al. (2017). Dendritic cytoskeletal architecture is modulated by combinatorial transcriptional regulation in *Drosophila melanogaster*. Genetics *207*, 1401–1421.

Davidson, A.J., Millard, T.H., Evans, I.R., and Wood, W. (2019). Ena orchestrates remodelling within the actin cytoskeleton to drive robust *Drosophila* macrophage chemotaxis. J. Cell Sci. *132*, jcs.224618.

Dimitrova, S., Reissaus, A., and Tavosanis, G. (2008). Slit and Robo regulate dendrite branching and elongation of space-filling neurons in Drosophila. Dev. Biol. *324*, 18–30.

Ferreira, T., Ou, Y., Li, S., Giniger, E., and van Meyel, D.J. (2014). Dendrite architecture organized by transcriptional control of the F-actin nucleator Spire. Development *141*, 650–660.

Ferreira Castro, A., Baltruschat, L., Stürner, T., Bahrami, A., Jedlicka, P., Tavosanis, G., and Cuntz, H. (2020). Achieving functional neuronal dendrite structure through sequential stochastic growth and retraction. Elife *9*, e60920.

Flynn, K.C., Hellal, F., Neukirchen, D., Jacob, S., Tahirovic, S., Dupraz, S., Stern, S., Garvalov, B.K., Gurniak, C., Shaw, A.E., et al. (2012). ADF/cofilin-mediated actin retrograde flow directs neurite formation in the developing brain. Neuron *76*, 1091–1107.

Gao, F.-B., and Bogert, B.A. (2003). Genetic control of dendritic morphogenesis in Drosophila. Trends Neurosci. *26*, 262–268.

Gao, F.-B., Brenman, J.E., Jan, L.Y., and Jan, Y.N. (1999). Genes regulating dendritic outgrowth, branching, and routing in Drosophila. Genes Dev. *13*, 2549–2561.

Grueber, W.B., Jan, L.Y., and Jan, Y.N. (2002). Tiling of the Drosophila epidermis by multidendritic sensory neurons. Dev. Camb. Engl. *129*, 2867–2878.

Grueber, W.B., Jan, L.Y., and Jan, Y.N. (2003). Different levels of the homeodomain protein cut regulate distinct dendrite branching patterns of Drosophila multidendritic neurons. Cell *112*, 805–818.

Gunsalus, K.C., Bonaccorsi, S., Williams, E., Verni, F., Gatti, M., and Goldberg, M.L. (1995). Mutations in twinstar, a Drosophila gene encoding a cofilin/ADF homologue, result in defects in centrosome migration and cytokinesis. J. Cell Biol. *131*, 1243–1259.

Hansen, S.D., and Mullins, R.D. (2010). VASP is a processive actin polymerase that requires monomeric actin for barbed end association. J. Cell Biol. *191*, 571–584.

Hogg, P.W., Coleman, P., Dellazizzo Toth, T., and Haas, K. (2021). Quantifying neuronal structural changes over time using dynamic morphometrics. Trends Neurosci. *45*, 106–119.

Hotulainen, P., and Lappalainen, P. (2006). Stress fibers are generated by two distinct actin assembly mechanisms in motile cells. J. Cell Biol. *173*, 383–394.

Hoyer, N., Zielke, P., Hu, C., Petersen, M., Sauter, K., Scharrenberg, R., Peng, Y., Kim, C.C., Han, C., Parrish, J.Z., et al. (2018). Ret and substrate-derived TGF-β maverick regulate space-filling dendrite growth in Drosophila sensory neurons. Cell Rep. *24*, 2261–2272.e5.

Jan, Y.-N., and Jan, L.Y. (2010). Branching out: mechanisms of dendritic arborization. Nat. Rev. Neurosci. *11*, 316–328.

Kanaoka, Y., Skibbe, H., Hayashi, Y., Uemura, T., and Hattori, Y. (2019). DeTerm: software for automatic detection of neuronal dendritic branch terminals via an artificial neural network. Genes Cells *24*, 464–472.

Koene, R.A., Tijms, B., van Hees, P., Postma, F., de Ridder, A., Ramakers, G.J.A., van Pelt, J., and van Ooyen, A. (2009). NETMORPH: a framework for the stochastic generation of large scale neuronal networks with realistic neuron morphologies. Neuroinformatics *7*, 195–210.

Koestler, S.A., Steffen, A., Nemethova, M., Winterhoff, M., Luo, N., Holleboom, J.M., Krupp, J., Jacob, S., Vinzenz, M., Schur, F., et al. (2013). Arp2/3 complex is essential for actin network treadmilling as well as for targeting of capping protein and cofilin. Mol. Biol. Cell *24*, 2861–2875.

Konietzny, A., Bär, J., and Mikhaylova, M. (2017). Dendritic actin cytoskeleton: structure, functions, and regulations. Front. Cell. Neurosci. *11*, 147.

Kovar, D.R., Harris, E.S., Mahaffy, R., Higgs, H.N., and Pollard, T.D. (2006). Control of the assembly of ATP- and ADP-actin by formins and profilin. Cell *124*, 423–435.

Krause, M., Bear, J.E., Loureiro, J.J., and Gertler, F.B. (2002). The Ena/VASP enigma. J. Cell Sci. *115*, 4721–4726.

Lai, F.P., Szczodrak, M., Block, J., Faix, J., Breitsprecher, D., Mannherz, H.G., Stradal, T.E., Dunn, G.A., Small, J.V., and Rottner, K. (2008). Arp2/3 complex interactions and actin network turnover in lamellipodia. EMBO J. *27*, 982–992.

Lanoue, V., and Cooper, H.M. (2019). Branching mechanisms shaping dendrite architecture. Dev. Biol. *451*, 16–24.

Lee, T., and Luo, L. (1999). Mosaic analysis with a repressible cell marker for studies of gene function in neuronal morphogenesis. Neuron *22*, 451–461.

Li, Y., Wang, D., Ascoli, G.A., Mitra, P., and Wang, Y. (2017). Metrics for comparing neuronal tree shapes based on persistent homology. PLoS One *12*, e0182184.

Long, H., Ou, Y., Rao, Y., and van Meyel, D.J. (2009). Dendrite branching and self-avoidance are controlled by Turtle, a conserved IgSF protein in *Drosophila*. Development *136*, 3475–3484.

MacNeil, M.A., and Masland, R.H. (1998). Extreme diversity among amacrine cells: implications for function. Neuron *20*, 971–982.

Mallavarapu, A., and Mitchison, T. (1999). Regulated actin cytoskeleton assembly at filopodium tips controls their extension and retraction. J. Cell Biol. *146*, 1097–1106.

Marchenko, O.O., Das, S., Yu, J., Novak, I.L., Rodionov, V.I., Efimova, N., Svitkina, T., Wolgemuth, C.W., and Loew, L.M. (2017). A minimal actomyosin-based model predicts the dynamics of filopodia on neuronal dendrites. Mol. Biol. Cell *28*, 1021–1033.

Memelli, H., Torben-Nielsen, B., and Kozloski, J. (2013). Self-referential forces are sufficient to explain different dendritic morphologies. Front. Neuroinf. *7*, 1.

Mogilner, A., and Oster, G. (1996). Cell motility driven by actin polymerization. Biophys. J. *71*, 3030–3045.

Mogilner, A., and Rubinstein, B. (2005). The physics of filopodial protrusion. Biophys. J. *89*, 782–795.

Mullins, R.D., Heuser, J.A., and Pollard, T.D. (1998). The interaction of Arp2/3 complex with actin: nucleation, high affinity pointed end capping, and formation of branching networks of filaments. Proc. Natl. Acad. Sci. *95*, 6181–6186.

Nagel, J., Delandre, C., Zhang, Y., Förstner, F., Moore, A.W., and Tavosanis, G. (2012). Fascin controls neuronal class-specific dendrite arbor morphology. Development *139*, 2999–3009.

Nanda, S., Chen, H., Das, R., Bhattacharjee, S., Cuntz, H., Torben-Nielsen, B., Peng, H., Cox, D.N., De Schutter, E., and Ascoli, G.A. (2018a). Design and implementation of multi-signal and time-varying neural reconstructions. Sci. Data *5*, 170207.

Nanda, S., Das, R., Bhattacharjee, S., Cox, D.N., and Ascoli, G.A. (2018b). Morphological determinants of dendritic arborization neurons in Drosophila larva. Brain Struct. Funct. *223*, 1107–1120.

Nanda, S., Bhattacharjee, S., Cox, D.N., and Ascoli, G.A. (2020). Distinct relations of microtubules and actin filaments with dendritic architecture. iScience *23*, 101865.

Nithianandam, V., and Chien, C.-T. (2018). Actin blobs prefigure dendrite branching sites. J. Cell Biol. *217*, 3731–3746.

Palavalli, A., Tizón-Escamilla, N., Rupprecht, J.-F., and Lecuit, T. (2021). Deterministic and stochastic rules of branching govern dendrite morphogenesis of sensory neurons. Curr. Biol. *31*, 459–472.e4.

Parrish, J.Z., Xu, P., Kim, C.C., Jan, L.Y., and Jan, Y.N. (2009). The microRNA bantam functions in epithelial cells to regulate scaling growth of dendrite arbors in Drosophila sensory neurons. Neuron *63*, 788–802.

Pasic, L., Kotova, T., and Schafer, D.A. (2008). Ena/VASP proteins capture actin filament barbed ends. J. Biol. Chem. *283*, 9814–9819.

Poe, A.R., Tang, L., Wang, B., Li, Y., Sapar, M.L., and Han, C. (2017). Dendritic space-filling requires a neuronal type-specific extracellular permissive signal in *Drosophila*. Proc. Natl. Acad. Sci. U S A *114*, E8062–E8071.

Poirazi, P., and Papoutsi, A. (2020). Illuminating dendritic function with computational models. Nat. Rev. Neurosci. *21*, 303–321.

Portera-Cailliau, C., Pan, D.T., and Yuste, R. (2003). Activity-regulated dynamic behavior of early dendritic protrusions: evidence for different types of dendritic filopodia. J. Neurosci. *23*, 7129–7142.

Pruyne, D., Evangelista, M., Yang, C., Bi, E., Zigmond, S., Bretscher, A., and Boone, C. (2002). Role of formins in actin assembly: nucleation and barbed-end association. Science *297*, 612–615.

Quinlan, M.E., Hilgert, S., Bedrossian, A., Mullins, R.D., and Kerkhoff, E. (2007). Regulatory interactions between two actin nucleators, Spire and Cappuccino. J. Cell Biol. *179*, 117–128.

Röper, K., Mao, Y., and Brown, N.H. (2005). Contribution of sequence variation in *Drosophila* actins to their incorporation into actin-based structures *in vivo*. J. Cell Sci. *118*, 3937–3948.

Santos, T.E., Schaffran, B., Broguière, N., Meyn, L., Zenobi-Wong, M., and Bradke, F. (2020). Axon growth of CNS neurons in three dimensions is amoeboid and independent of adhesions. Cell Rep. *32*, 107907.

Schaks, M., Giannone, G., and Rottner, K. (2019). Actin dynamics in cell migration. Essays Biochem. *63*, 483–495.

Schneider, C.A., Rasband, W.S., and Eliceiri, K.W. (2012). NIH Image to ImageJ: 25 years of image analysis. Nat. Methods *9*, 671–675.

Sheng, C., Javed, U., Gibbs, M., Long, C., Yin, J., Qin, B., and Yuan, Q. (2018). Experience-dependent structural plasticity targets dynamic filopodia in regulating dendrite maturation and synaptogenesis. Nat. Commun. *9*, 3362.

Shepherd, D., and Smith, S.A. (1996). Central projections of persistent larval sensory neurons prefigure adult sensory pathways in the CNS of *Drosophila*. Development *112* (*8*), 2375–2384. https://doi.org/10.1242/dev.122.8.2375.

Shimono, K., Fujishima, K., Nomura, T., Ohashi, M., Usui, T., Kengaku, M., Toyoda, A., and Uemura, T. (2015). An evolutionarily conserved protein CHORD regulates scaling of dendritic arbors with body size. Sci. Rep. *4*, 4415.

Shukla, V.K., Maheshwari, D., Jain, A., Tripathi, S., Kumar, D., and Arora, A. (2018). Structure, dynamics, and biochemical characterization of ADF/cofilin twinstar from Drosophila melanogaster. Biochim. Biophys. Acta BBA - Protein Proteomics *1866*, 885–898.

Smith, B.A., Daugherty-Clarke, K., Goode, B.L., and Gelles, J. (2013). Pathway of actin filament branch formation by Arp2/3 complex revealed by single-molecule imaging. Proc. Natl. Acad. Sci. *110*, 1285–1290.

Star, E.N., Kwiatkowski, D.J., and Murthy, V.N. (2002). Rapid turnover of actin in dendritic spines and its regulation by activity. Nat. Neurosci. *5*, 239–246.

Stürner, T., Tatarnikova, A., Mueller, J., Schaffran, B., Cuntz, H., Zhang, Y., Nemethova, M., Bogdan, S., Small, V., and Tavosanis, G. (2019). Transient localization of the Arp2/3 complex initiates neuronal dendrite branching in vivo. Dev. Camb. Engl. *146*, dev171397.

Sugimura, K., Shimono, K., Uemura, T., and Mochizuki, A. (2007). Self-organizing mechanism for development of space-filling neuronal dendrites. PLoS Comput. Biol. *3*, e212.

Suraneni, P., Rubinstein, B., Unruh, J.R., Durnin, M., Hanein, D., and Li, R. (2012). The Arp2/3 complex is required for lamellipodia extension and directional fibroblast cell migration. J. Cell Biol. *197*, 239–251.

Svitkina, T., Lin, W.-H., Webb, D.J., Yasuda, R., Wayman, G.A., Van Aelst, L., and Soderling, S.H. (2010). Regulation of the postsynaptic cytoskeleton: roles in development, plasticity, and disorders. J. Neurosci. Off. J. Soc. Neurosci. *30*, 14937–14942.

Tavosanis, G. (2021). Dendrite enlightenment. Curr. Opin. Neurobiol. *69*, 222–230.

Torben-Nielsen, B., and De Schutter, E. (2014). Context-aware modeling of neuronal morphologies. Front. Neuroanat. *8*, 92.

Tsubouchi, A., Caldwell, J.C., and Tracey, W.D. (2012). Dendritic filopodia, ripped pocket, NOMPC, and NMDARs contribute to the sense of touch in Drosophila larvae. Curr. Biol. *22*, 2124–2134.

Turner, H.N., Armengol, K., Patel, A.A., Himmel, N.J., Sullivan, L., Iyer, S.C., Bhattacharya, S., Iyer, E.P.R., Landry, C., Galko, M.J., et al. (2016). The TRP channels Pkd2, NompC, and Trpm act in cold-sensing neurons to mediate unique aversive behaviors to noxious cold in Drosophila. Curr. Biol. *26*, 3116–3128.

Verkhusha, V.V., Tsukita, S., and Oda, H. (1999). Actin dynamics in lamellipodia of migrating border cells in the *Drosophila* ovary revealed by a GFP-actin fusion protein. FEBS Lett. *445*, 395–401.

Vignjevic, D., Kojima, S., Aratyn, Y., Danciu, O., Svitkina, T., and Borisy, G.G. (2006). Role of fascin in filopodial protrusion. J. Cell Biol. *174*, 863–875.

Wang, S., Tanzi, R.E., and Li, A. (2019). Quantitative analysis of neuronal dendritic arborization complexity in Drosophila. J. Vis. Exp. *143*, 57139.

Wang, Y.-H., Ding, Z.-Y., Cheng, Y.-J., Chien, C.-T., and Huang, M.-L. (2020). An efficient screen for cell-intrinsic factors identifies the chaperonin CCT and multiple conserved mechanisms as mediating dendrite morphogenesis. Front. Cell. Neurosci. *14*, 577315.

Wen, Q., and Chklovskii, D.B. (2008). A cost–benefit analysis of neuronal morphology. J. Neurophysiol. *99*, 2320–2328.

Winkelman, J.D., Bilancia, C.G., Peifer, M., and Kovar, D.R. (2014). Ena/VASP Enabled is a highly processive actin polymerase tailored to self-assemble parallel-bundled F-actin networks with Fascin. Proc. Natl. Acad. Sci. U S A *111*, 4121–4126.

Wolterhoff, N., Gigengack, U., and Rumpf, S. (2020). PP2A phosphatase is required for dendrite pruning via actin regulation in *Drosophila*. EMBO Rep. *21*, e48870.

Wu, C., Asokan, S.B., Berginski, M.E., Haynes, E.M., Sharpless, N.E., Griffith, J.D., Gomez, S.M., and Bear, J.E. (2012). Arp2/3 is critical for lamellipodia and response to extracellular matrix cues but is dispensable for chemotaxis. Cell *148*, 973–987.

Xie, Q., Brbic, M., Horns, F., Kolluru, S.S., Jones, R.C., Li, J., Reddy, A.R., Xie, A., Kohani, S., Li, Z., et al. (2021). Temporal evolution of single-cell transcriptomes of Drosophila olfactory projection neurons. Elife *10*, e63450.

Yalgin, C., Ebrahimi, S., Delandre, C., Yoong, L.F., Akimoto, S., Tran, H., Amikura, R., Spokony, R., Torben-Nielsen, B., White, K.P., et al. (2015). Centrosomin represses dendrite branching by orienting microtubule nucleation. Nat. Neurosci. *18*, 1437–1445.

Yan, Z., Zhang, W., He, Y., Gorczyca, D., Xiang, Y., Cheng, L.E., Meltzer, S., Jan, L.Y., and Jan, Y.N. (2013). Drosophila NOMPC is a mechanotransduction channel subunit for gentle-touch sensation. Nature *493*, 221–225.

Zito, K., Knott, G., Shepherd, G.M.G., Shenolikar, S., and Svoboda, K. (2004). Induction of spine growth and synapse formation by regulation of the spine actin cytoskeleton. Neuron *44*, 321–334.

STAR★METHODS

KEY RESOURCES TABLE

REAGENT or RESOURCE	SOURCE	IDENTIFIER
Experimental models: Organisms/strains		
D. melanogaster: P{ry[+t7.2] = hsFLP}12, y[1] w[*]; Arpc1[Q25sd] P{ry[+t7.2] = neoFRT}40A/CyO	Bloomington Drosophila Stock Center	BDSC: 9137
D. melanogaster: spir[1] cn[1] bw[1]/CyO, l(2)DTS513[1]	Bloomington Drosophila Stock Center	BDSC: 5113
D. melanogaster: b[1] pr[1] spir[2F] cn[1]/CyO	Bloomington Drosophila Stock Center	BDSC: 8723
D. melanogaster: M{UAS-spir.ORF.3xHA}ZH-86Fb	FlyORF	F001174
D. melanogaster: capu[1] cn[1] bw[1]/CyO, l(2)DTS513[1]	Bloomington Drosophila Stock Center	BDSC: 5094
D. melanogaster: capu[EE] cn[1] bw[1]/CyO	Bloomington Drosophila Stock Center	BDSC: 8788
D. melanogaster: P{pUAST-capu.mCherry}	This study	N/A
D. melanogaster: sn[3]	Bloomington Drosophila Stock Center	BDSC: 113
D. melanogaster: w[*]; P{w[+mW.hs] = FRT(w[hs])}G13 ena[210]/CyO	Bloomington Drosophila Stock Center	BDSC: 25404
D. melanogaster: w[*]; P{w[+mW.hs] = FRT(w[hs])}G13 tsr[N121]/CyO	Bloomington Drosophila Stock Center	BDSC: 9109
D. melanogaster: y[1] w[*]; P{w[+mC] = tubP-GAL80}LL10 P{ry[+t7.2] = neoFRT}40A/CyO	Bloomington Drosophila Stock Center	BDSC: 5192
D. melanogaster: w[*]; P{w[+mW.hs] = GawB}smid[C161]/TM6B, Tb[1]	Bloomington Drosophila Stock Center	BDSC: 27893
D. melanogaster: y[1] w[*]; Pin[Yt]/CyO; P{w[+mC] = UAS-mCD8::GFP.L}LL6	Bloomington Drosophila Stock Center	BDSC: 5130
D. melanogaster: w[*]; P{w[+mC] = UASp-GFP.Act5C}2-1	Bloomington Drosophila Stock Center	BDSC: 9258
D. melanogaster: UAS−mCD8−Cherry/TM3	Provided by Takashi Suzuki	N/A
D. melanogaster: P{w[+m] = GAL4}5–40 P{w[+mC] = UAS-Venus.pm}1 P{w[+mC] = SOP-FLP}42; P{w[+mC] = tubP-GAL80}LL10 P{ry[+t7.2] = neoFRT}40A/CyO*	Kyoto Stock Center	DGRC: 109947
D. melanogaster: P{w[+m] = GAL4}5–40 P{w[+mC] = UAS-Venus.pm}1 P{w[+mC] = SOP-FLP}42; P{w[+mW.hs] = FRT(w[hs])}G13 P{w[+mC] = tubP-GAL80}LL2/CyO*	Kyoto Stock Center	DGRC: 109948
D. melanogaster: w[*]; P{w[+mW.hs] = FRT(w[hs])}G13	Kyoto Stock Center	DGRC: 106602
D. melanogaster: w[1118]; P{ry[+t7.2] = neoFRT}40A/CyO; P{ry[+t7.2] = neoFRT}80B	Bloomington Drosophila Stock Center	BDSC: 8215
Deposited data		
Experimental data, neuron images and tracings	This study	Zenodo: https://doi.org/10.5281/zenodo.6347438
Software and algorithms		
Code used for analysis and modeling	This study	Zenodo: https://doi.org/10.5281/zenodo.6347438
TREES toolbox	Cuntz et al., 2010	https://www.treestoolbox.org/
MATLAB	Version 2017b	https://se.mathworks.com/products/matlab
ImageJ	Schneider et al., 2012	https://imagej.net
GraphPad Prism	Version 07	https://www.graphpad.com/

RESOURCE AVAILABILITY

Lead contact

Further information and requests for resources and reagents should be directed to and will be fulfilled by the lead contact, Prof. Dr. Gaia Tavosanis (gaia.tavosanis@dzne.de). For additional information about the code and modeling please contact Dr. Hermann Cuntz (cuntz@fias.uni-frankfurt.de).

Materials availability

All unique/stable reagents generated in this study are available from the lead contact without restriction.

Data and code availability

- All data reported in the paper have been deposited at Zenodo and are publicly available as of the date of publication. DOIs are listed in the key resources table.
- All original code has been deposited at Zenodo and is publicly available as of the date of publication. DOIs are listed in the key resources table.
- Any additional information required to reanalyse the data reported in this paper is available from the lead contact upon request.

EXPERIMENTAL MODEL AND SUBJECT DETAILS

Fly strains

Flies were reared on standard food in a 12hr light-dark cycle at 25°C and 60% humidity unless otherwise indicated.

A pUAST (Brand and Perrimon, 1993) containing a full-length Capu construct with a mCherry fluorescent tag (Q24120, 1059 aa) (kindly provided by Annette Samol-Wolf and Prof. Dr. Eugen Kerkhoff) was injected by BestGene Inc. (Chino Hills, CA, USA) to the 3rd Chromosome.

METHOD DETAILS

Microscopy/live imaging

For all of the imaging in this work living larvae were covered in Halocarbon oil, to allow oxygen exchange and immobilised between a coverslip and a glass slide. After imaging larvae were checked for vitality and set back on fly food, images taken from larvae that did not survive until hatching were excluded from the analysis. The larvae were placed on their side to allow the imaging of the same lateral c3da neuron (ldaB) of the abdominal segment A5.

In the FRAP experiments the same anterior portion of the ldaB neuron of late second instar larva were imaged with an LSM 800 Airyscan Microscope and a 63 ×/1.40 oil objective (Figure 2A). A 488nm for GFP and 561nm for mCherry line of an argon laser was used. The frame, including the ROI (tip of a branchlet), was imaged at least three times before bleaching. The laser was set to 90% maximal power for bleaching and 2% maximal power for imaging. Photo-bleaching was achieved with 10 iterations (scan speed at 3) of the region of interest. Imaging of the area was resumed immediately after photo-bleaching and continued every 30sec for at least ∼ 300sec.

For Figures 2 and S2 the entire dendritic tree of early third instar *Drosophila melanogaster* larvae were imaged with an LSM 780 Zeiss 40× oil objective, the software used was ZEN 2010. One neuron was imaged per animal, 8 animals per genotype were used for Figures 2 and 5 animals were used for Figure S2. The *capu*^{1}/*spire*^{2F} transheterozygous mutant was imaged in the same way and only 5 animals were used.

For the time-lapse series in Figure 6 over 30min every 30sec was taken of an anterior portion of the ldaB neuron of late second instar larva with a Yokogawa Spinning-Disc on a Nikon stand (Andor, Oxford UK) with two back-illuminated EM-CCD cameras (Andor iXON DU-897) and a 60× oil objective. One neuron was imaged per animal, 10 animals per genotype.

FRAP analysis

For the FRAP analyses *w[*]; P{w[+mW.hs] = GawB}smid[C161]/TM6B, Tb[1]* (B#27893) (Shepherd and Smith, 1996) was recombined with *UAS−mCD8−Cherry/TM3* (kindly provided by Takashi Suzuki) and crossed to *w[*]; P{w[+mC] = UASp-GFP.Act5C}2-1* (B# 9258).

A line analysis was conducted in the ImageJ software (version 1.52a) over time and space with a short macro that measures the intensity (I_{GFP}, $I_{mCherry}$) of each pixel of the two channels along the line over time. Moreover, it tracks the extension of the branch along the line by comparing the intensity to an adjustable threshold (script: *Analysis_FRAP_macro*).

Background fluorescence intensities (I_{GFPbg}, $I_{mCherrybg}$) taken from a region outside the cell were subtracted from each individual region and frame. The values were normalised to the average of 3 pre-bleach values (I_N). Acquisition photo bleaching was determined by comparing the normalised mCherry signal (ImCherry) in the bleached area over time, the area seems unaffected by experimental bleaching as there is even an increase in mCherry signal over time. In Figure 2D the normalised GFP fluorescence ($I = \frac{I_{GFP} - I_{GFPbg}}{I_N}$) is

visualised over time. Time point 0 (t_0) was defined at the first time point after photo bleaching (after 2min) and the last time point as the $t\infty$. The average half-time recovery was calculated $I_{1/2} = (I_\infty + I_0)/2$ and the time point closest was defined as $t_{1/2}$. The average retrograde movement of actin (M) was quantified by drawing a line at the distance the pixel below a 30% Intensity threshold had from the originally bleached area toward the MB. There is a very slow retrograde movement of $M = 0.13$ μm/min ($SD = 0.04$).

Dendritic arbor analysis

Eight image stacks per genotype were manually reconstructed in 3D using the user interface *cgui_tree* of the *TREES toolbox* (www.treestoolbox.org) (Cuntz et al., 2010), an open source software package for MATLAB (Matworks, Natick, MA). A large palette of 30 branching statistics (Table 2) specifically for the c3da neurons were collected for each set of dendrite reconstructions using TREES toolbox functions. These branching statistics are aggregated in our new *features_c3_tree* function.

Each mutant looked at in this study has a unique code of features which are significantly altered in comparison to the corresponding control. The Table S1 shows the corrected p values for each feature in each mutant. For Figure 4 we were only interested in features that would help us detect the differences between the six mutants. Therefore, any feature that was altered in all or none of the mutants was excluded. From the remaining features we decided to concentrate on the ones that were not a combination of two or more of the other features. For example, we excluded the feature Density ($density = \frac{total\ length}{surface}$) because we had already included the total length and the surface area.

Time-lapse analysis

Ten image series per genotype were analyzed. The single images of the 30min time series were manually reconstructed in 2D using the user interface *cgui_tree* of the TREES toolbox (www.treestoolbox.org) (Cuntz et al., 2010) every 5min. Then they were registered using the *ui_tlbp_tree* script as described in Baltruschat et al. (2020) tracking terminal and branch points. The eval time-lapse script categorises the STBs into 5 groups: new branches that appear throughout the 30min and disappearing branches, branches with are extending or retracting and branches that do not change in length within a certain threshold (resolution captured by the microscope). These numbers were divided by the total number of branches within the image frame. This allowed us to compare the different mutants and the branch dynamics independently of their difference in total branch number at the beginning of the imaging session. Moreover, the eval time-lapse script computes the velocity of branch movement, as the average distance covered by an STB over time (*script_time-lapse_analysis*). This analysis was developed in parallel to the time-lapse analysis in Ferreira Castro et al. (2020).

Computational modeling

The SFGT neuron model was described previously in Baltruschat et al. (2020) and is provided there as a TREES Toolbox function growth tree. Briefly, the SFGT model grows branches in several iterations starting from the root location, the cell soma position of a given neuron, and it stays within the spanning field taken from that neuron. At each growth iteration, a new target is selected within the dendritic spanning field but far away from the existing tree. A parameter k determines the stochasticity of the selection of the new target with a value of 0 referring to the target being as far as possible from the existing tree without any noise and 1 the target being chosen completely at random. A balancing factor bf weighs total cable length cost against mean path length to the soma (Cuntz et al., 2007, 2010). A parameter radius determines the outreach threshold that a new branch can grow to, restricting the area in which a target can be selected. This model was obtained from developmental growth iterations in time-lapse images and reproduces both the c4da morphology accurately as well as –though with different parameters– the morphology of a large number of dendrites from other cell types. The c4da model parameters were k = 0.45, bf = 0.225 and radius = 120μm. In comparison, the model matching c3da MBs in this work was rather similar with k = 0.15, bf = 0.1 and radius = 100μm.

The SFGT model by Baltruschat et al. (2020) was manually fitted to reproduce the MBs in the wild-type c3da neurons as described above (Figure 3A). In order to just model the MBs the growth was first interrupted when the dendrite reached the number of MB terminals in the real counterpart. The resulting dendritic total length served as a reference for finding good parameters. To account for synthetic morphologies grown in a given spanning field being systematically smaller than the original trees, the resulting model dendrites were slightly scaled to match the spanning field of their real counterparts.

In Figure S1 a similar routine was repeated with the MST algorithm instead of the SFGT program. Importantly, the MST model was applied with the same parameters as the SFGT model showing their equivalence. This was done by distributing targets randomly within the spanning field of the original reconstructions. Targets were connected with the MST_tree function of the TREES Toolbox with bf = 0.1 (Cuntz et al., 2010). The number of targets was selected so that the model tree just reached the same number of terminals as the original tree. In other words, the parameters were manually fitted in the SFGT model to the wild-type c3da neurons but matched adequately the MST results. In both cases the resulting morphologies were scaled to fill the same spanning field as the data (Figure S1A).

Since the characteristic STBs of c3da dendrites were not well captured by the SFGT model (Figure 1B) nor by the MST model (Figure S1B), we implemented a transition to a second growth program after the MBs had completed their extension. STBs were modeled by exploring which minimal changes needed to be introduced to the SFGT model to obtain realistic total dendrite length, branch length distributions and distributions of STBs along the path from soma to the dendrite tip.

One viable model for the second growth step was found by restricting the reach of the targets to a close distance from the existing dendrite. This reach was inversely correlated with the local dendrite diameter D by 4.2μm – D. A stochasticity of the reach values was obtained by multiplying the reach by noise of 1μm ± 6μm low pass filtered with a Gaussian filter with a 60μm length constant. The reach was finally scaled by ×3.4 and capped at 10μm while reach values below 4.2μm were set to 0μm resulting in the characteristic STB-less stretches along c3da dendrites. It is important to note that we do not believe that the two growth steps happen subsequently but rather that their dynamics are intertwined. Furthermore, the second growth step had different parameters with k = 0.5, bf = 0.625 and without any further radius = ∞μm. Most notably, the specific shape, angles and branch length distributions of STBs could only be reproduced when introducing a more fundamental change to the parameter bf. Here, instead of increasing cost with long paths to the dendrite root, the paths were measured in reference to the dendrite's MBs resulting in mostly unbranched STBs directed toward the main dendrite (Figures 1C and S1C).

Mutant synthetic morphologies were grown using exactly the same two-step growth program as used for the wild-type morphologies. The only differences in morphology therefore come from the specific differences in dendrite spanning fields as well as from the number of MBs and total number of branches.

QUANTIFICATION AND STATISTICAL ANALYSIS

Data were analyzed using Prism7.0 (GraphPad). Groups were compared using the Kruskal- Wallis test followed by Dunn's post hoc test accordingly. Single comparisons between two groups were analyzed using the two tailed Wilcoxon Signed Rank Test. For multiple comparisons with several features for each group the p values were controlled for false discovery rate by the adaptive method of Benjamini, Krieger and Yekutieli with a Q% of 1 (Benjamini et al., 2006) and controlled for statistical significance with the Holm-Sidak method (alpha of 0.05). Normal distribution of the dataset was confirmed using the Shapiro-Wilk and Kolmogorow-Smirnow normality test. The p values shown are all adjusted p values. (* is $p < 0.05$, ** is $p < 0.01$ and *** is $p < 0.001$).

Cell Reports, Volume *39*

Supplemental information

The branching code: A model of actin-driven dendrite arborization

Tomke Stürner, André Ferreira Castro, Maren Philipps, Hermann Cuntz, and Gaia Tavosanis

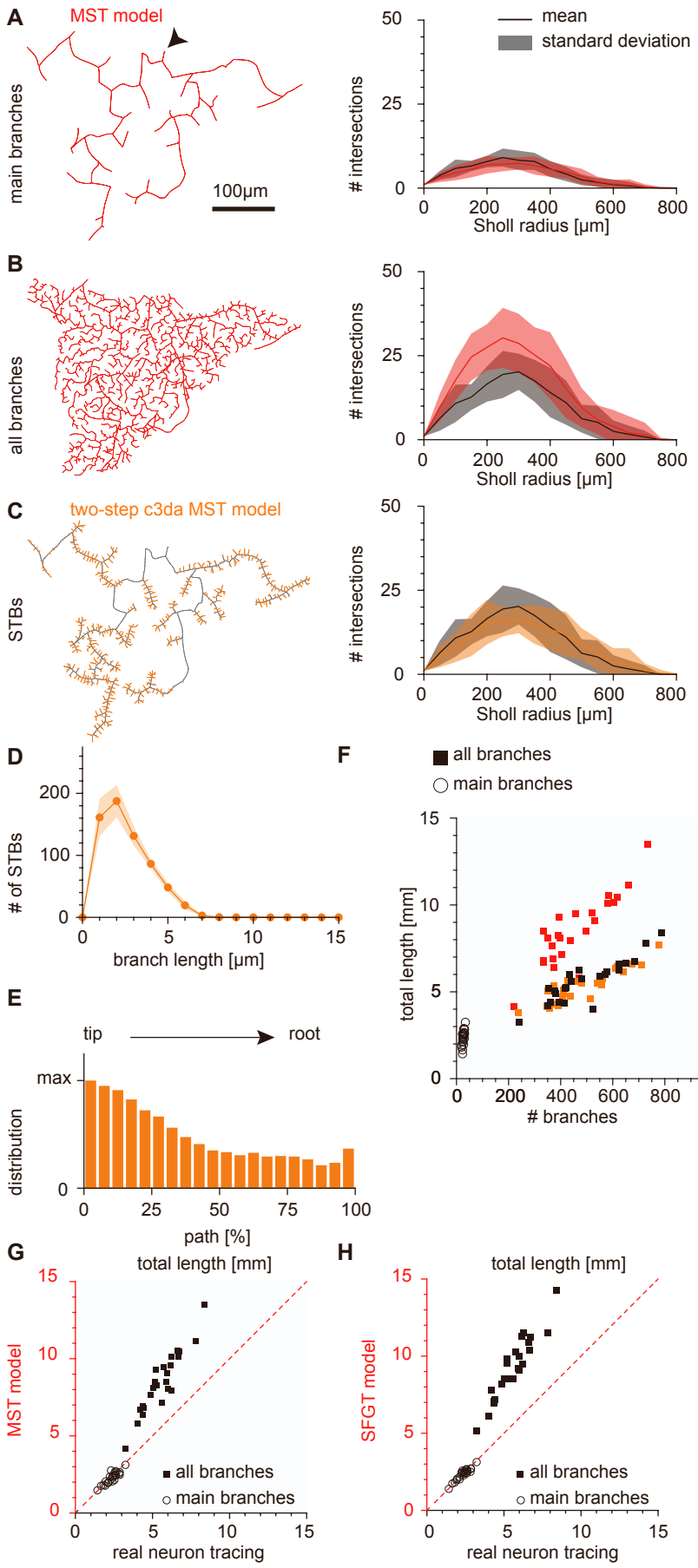

Fig S1. MST tree, Related to Figure 1

A,B,C, Synthetic dendritic trees (red or orange) focusing on the MBs (A), all branches (B) or the STBs (C) as seen in Figure 1 but now using the MST algorithm instead of the SFGT model. The arrowhead points to the root. Right hand Sholl analysis panels show the number of intersections of the dendritic trees with increasing Sholl radii around the soma in µm. Shaded area shows standard deviation. Solid lines show the mean Sholl intersections. The black line and grey shaded area show the data from tracings of a wild type c3da neuron as in Figure 1. A, B, The synthetic dendritic trees in red were generated with the MST algorithm (Cuntz et al., 2007), but the growth was interrupted either when the number of MBs (A) was reached or interrupted when the total number of branches (B) was reached. C, A second modelling step of the synthetic dendritic tree in orange allows STBs with a defined total length to develop in a close range to the MB with a given distribution along the MBs. D, The number of STBs in the synthetic trees obtained with the two-step model plotted against their length in µm. E, The number of STBs at positions along the MBs, from tip to root (depicted as a percentile of the path length). F, Number of branches vs. total length for MBs (empty dots) and complete trees (squares) are shown for real trees (black) compared to synthetic dendritic trees modelled with the MST (red) or the two-step model using the MST for the main branches (orange). G,H, Direct comparison of total length in mm between real neuron reconstructions and the MST model (G) or the SFGT model (H). See Materials and Methods for details.

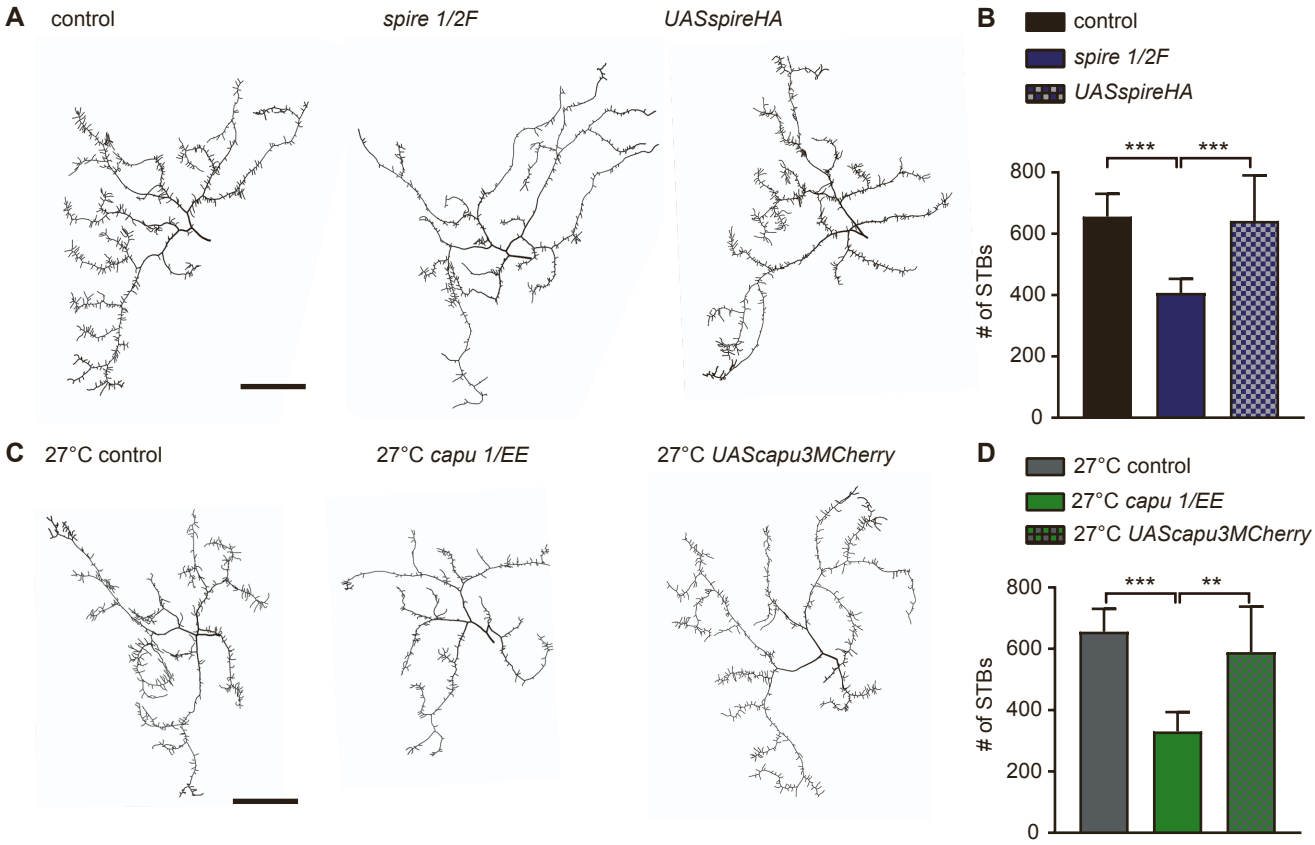

Fig S2. Spire and Capu Rescue, Related to Figure 3

A, Representative tracings of control, spire$^{1/2F}$ mutant and UASspirHA rescue. B, Quantification of STB number. C, Representative tracings of control, capu$^{1/EE}$ mutant and UAScapu3MCherry rescue. D, Quantification of branch number. (* is $p < 0.05$, ** is $p < 0.01$ and *** is $p < 0.001$). Mean with standard deviation. Scale bar is 100µm. n = 5 larva per genotype (see Table 1 for genotypes).

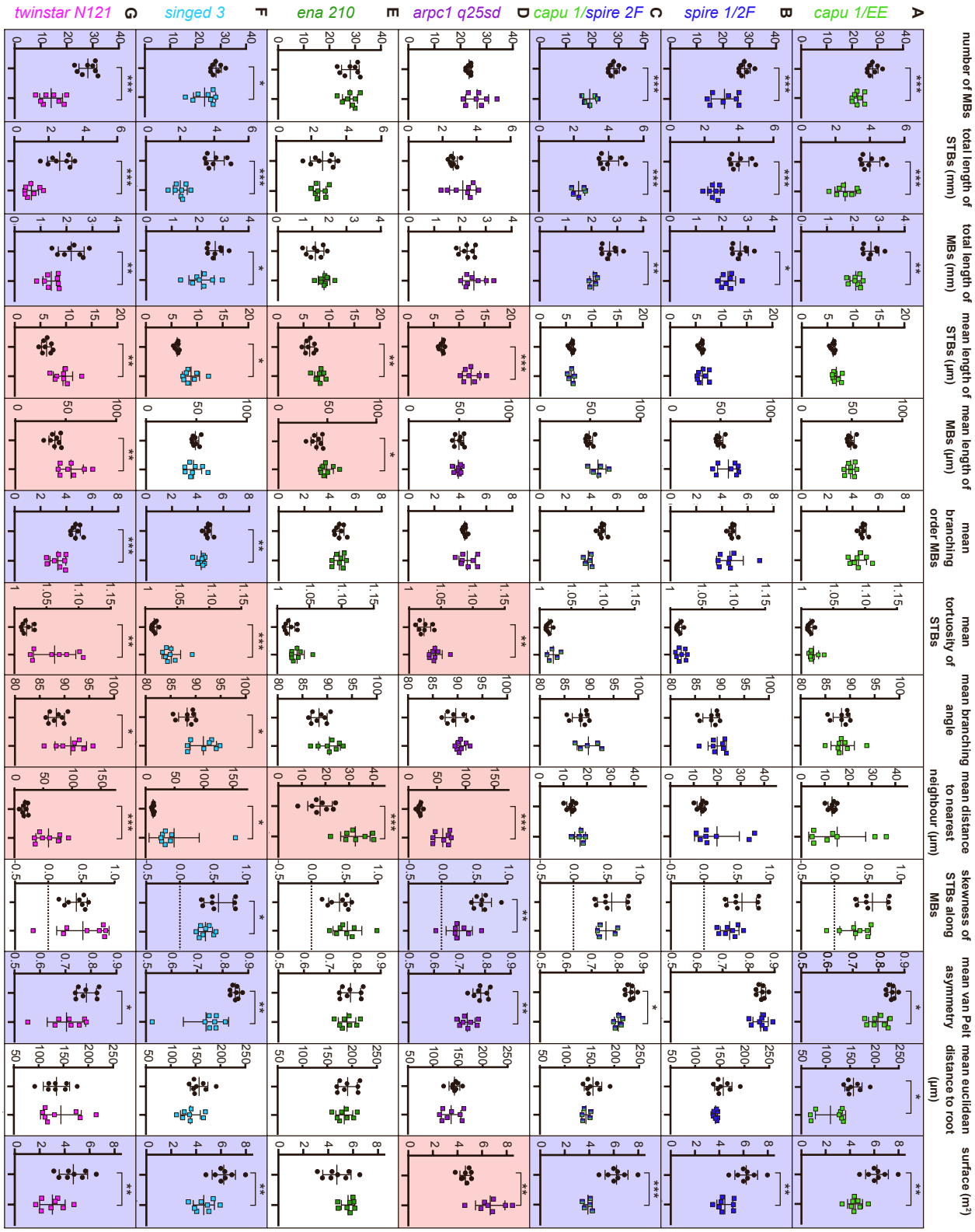

Fig S3. Morphological Analysis, Related to Figure 4

Thirteen morphological measurements for the c3da neurons. A-G, The thirteen measurements for each AMP mutant (and the capu^{1}/spire^{2F} heterozygous mutant) compared to corresponding controls. (Corrected p values * is $p < 0.05$, ** is $p < 0.01$ and *** is $p < 0.001$). Mean with standard deviation. The background is highlighted in blue for a significant decrease and in red for a significant increase. For a full list of corrected p values see Supplemental Table ST1, for full list of features and descriptions see Table 2 in Material and Methods. n = 8 for all apart from the heterozygous mutant capu^{1}/spire^{2F} which has a n = 5.

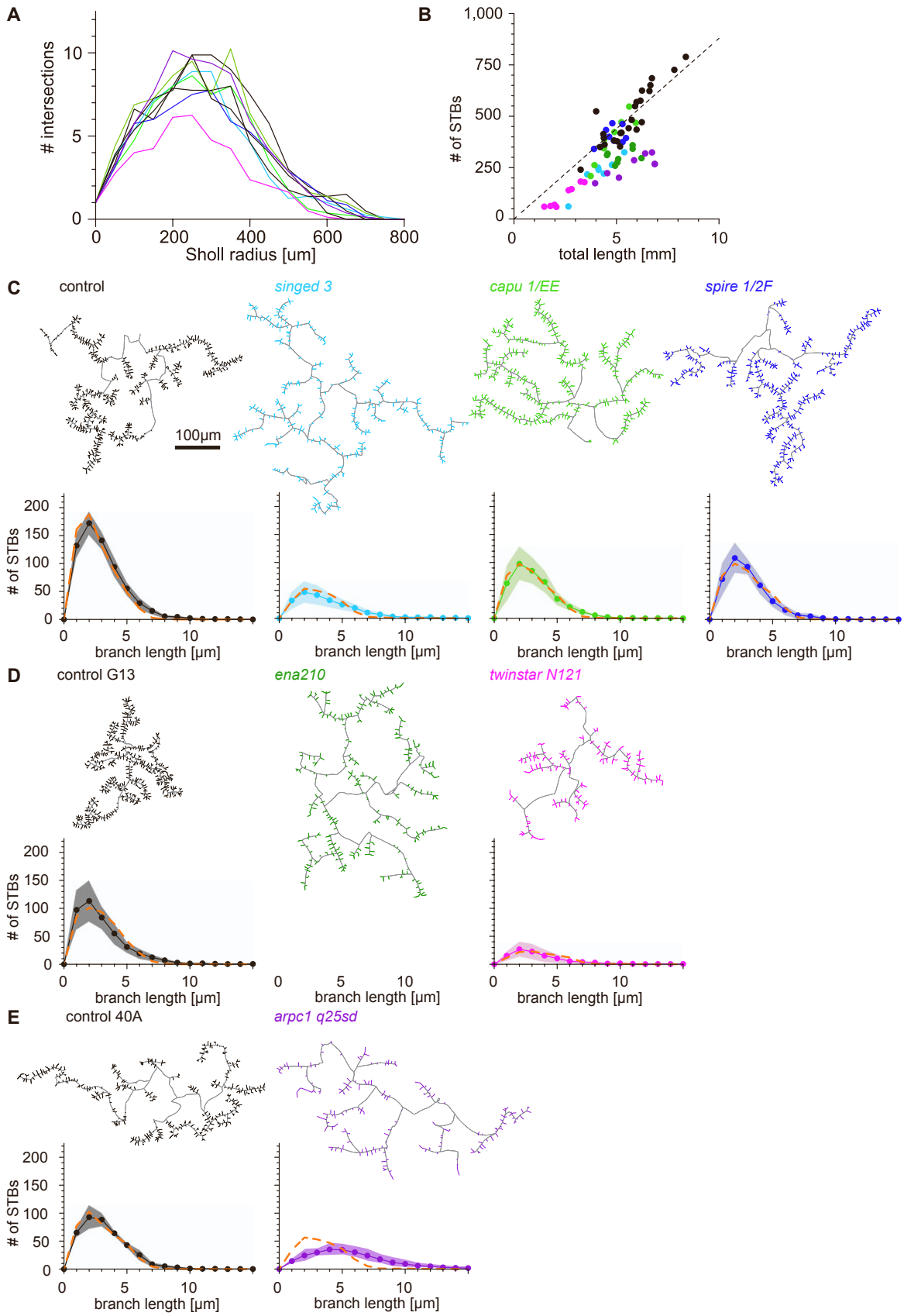

Fig S4. Further quantification of c3da neuron mutants and MST-based modelling version, Related to Figure 5

A, Sholl analysis of the MBs of control and mutant morphologies. B, The number of STBs against the total length for all controls and mutant tracings. C, D, E, The same representation as in Figure 5 but using the MST model for the main branches. Same colours as in Figure 5. For details see Material and Methods.

Table S1. Corrected p values for the 30 features, Related to Figure 4

Corrected p values for all six AMP mutants and all 30 dendrite features. The features shown in Figure 4 are in bold text. A note on the side gives the reason why the other feature were not used in the Figure 4, it states all, none or the number of the feature it correlates with. The background colour is red if there is a significant increase and blue if there was a significant decrease for the specific mutant condition. All trees, features and values are available in Zenodo (10.5281/zenodo.6347438).

#	Name	spire	capu	singed	twinstar	ena	arp	note
1	Number of STBs	<,001	<,001	<,001	<,001	0.03	<,001	all
2	**Number of MBs**	0.006	<,001	0.018	<,001	0.945	0.072	
3	**Total length of STBs**	<,001	0.001	<,001	<,001	0.644	0.072	
4	**Total length of MBs**	0.022	0.003	0.018	0.002	0.075	0.147	
5	**Mean length of STBs**	0.565	0.069	0.027	<,001	0.02	<,001	
6	**Mean length of MBs**	0.084	0.729	0.321	0.004	0.03	0.436	
7	**Mean branch order of MBs**	0.616	0.192	0.004	<,001	0.945	0.287	
8	**Mean tortuosity of STBs**	0.324	0.151	<,001	0.003	0.07	0.004	
9	**Mean branching angle**	0.223	0.657	0.011	0.024	0.093	0.191	
10	**Mean distance to nearest neighbour**	0.7	0.016	0.005	0.014	0.554	0.004	
11	**Skewness of STBs along MBs**	0.104	0.052	0.028	0.287	0.32	0.002	
12	**Mean van Pelt asymmetry**	0.113	0.057	0.024	<,001	0.004	<,001	
13	**Mean Euclidean distance to the root**	0.066	0.029	0.089	0.315	0.31	0.287	
14	**Surface**	0.003	0.002	0.004	0.006	0.115	0.001	
15	Mean branch order of STBs	0.05	0.016	<,001	<,001	0.036	<,001	all
16	Mean tortuosity of MBs	0.7	0.249	0.089	0.109	0.945	0.094	none
17	Number of branching points	<,001	<,001	<,001	<,001	0.03	<,001	all
18	Maximal branch length of STBs	0.223	0.656	0.011	0.012	0.03	0.001	see 5
19	Fraction of lengths of STBs / total length	0.012	0.021	<,001	<,001	0.036	0.272	see 3,4
20	Number of STBs / total length of MBs	<,001	0.007	<,001	<,001	0.03	<,001	all
21	Minimal branch length of MBs	0.7	0.46	0.335	0.315	0.516	0.486	none
22	Maximal branch length of MBs	0.134	0.617	0.081	0.127	0.144	0.508	none
23	Maximal branch order of MBs	0.026	0.029	0.018	<,001	0.91	0.484	see 7
24	Maximal branch order of STBs	0.134	0.021	<,001	<,001	0.093	0.003	see 15
25	Maximal Euclidean distance to the root	0.516	0.153	0.072	0.378	0.219	0.376	none
26	Mean Euclidean compactness	0.134	0.18	0.002	0.005	0.03	0.001	see 13,7
27	Maximal path distance to the root	0.789	0.228	0.08	0.228	0.219	0.147	none
28	Mean path distance to the root	0.516	0.037	0.072	0.399	0.093	0.376	see 13
29	Mean path compactness	0.104	0.258	0.002	0.006	0.03	0.003	see 13,7
30	Density	0.739	0.619	0.005	0.002	0.144	0.003	see 3,4,14